



Fairchild, I. J., Bonnand, P., Davies, T., Fleming, E. J., Grassineau, N., Halverson, G. P., Hambrey, M. J., McMillan, E. M., McKay, E., Parkinson, I. J., & Stevenson, C. T. E. (2016). The Late Cryogenian Warm Interval, NE Svalbard: Chemostratigraphy and genesis. *Precambrian Research*, 281, 128-154.
<https://doi.org/10.1016/j.precamres.2016.05.013>

Peer reviewed version

License (if available):
CC BY-NC-ND

Link to published version (if available):
[10.1016/j.precamres.2016.05.013](https://doi.org/10.1016/j.precamres.2016.05.013)

[Link to publication record in Explore Bristol Research](#)
PDF-document

This is the author accepted manuscript (AAM). The final published version (version of record) is available online via Elsevier at <http://www.sciencedirect.com/science/article/pii/S0301926816301577>. Please refer to any applicable terms of use of the publisher.

University of Bristol - Explore Bristol Research

General rights

This document is made available in accordance with publisher policies. Please cite only the published version using the reference above. Full terms of use are available:
<http://www.bristol.ac.uk/red/research-policy/pure/user-guides/ebr-terms/>

The Late Cryogenian Warm Interval, NE Svalbard: chemostratigraphy and genesis

Ian J. Fairchild^{a,1}, Pierre Bonnard^b, Tesni Davies^a, Edward J. Fleming^{a,c}, Nathalie Grassineau^d, Galen P. Halverson^e, Michael J. Hambrey^h, Emily M. McMillan^a, Elizabeth McKay^a, Ian J. Parkinsonⁱ, Carl T.E. Stevenson^a

^a*School of Geography, Earth and Environmental Sciences, University of Birmingham, Birmingham B15 2TT, UK*

^b*Department of Earth Sciences, South Parks Road, Oxford OX1 3AN, UK*

^c*CASP, West Building, 181A Huntingdon Road, Cambridge, CB3 0DH, UK*

^d*Department of Earth Sciences, Royal Holloway University of London, Egham, Surrey TW20 0EX, UK*

^g*Department of Earth and Planetary Sciences/Geotop, McGill University, 3450 University St., Montréal, QC, H3A 0E8, Canada*

^h*Department of Geography and Earth Sciences, Aberystwyth University, Aberystwyth, Ceredigion SY23 3DB, UK*

ⁱ*Department of Earth Sciences, University of Bristol, Wills Memorial Building, Queen's Road, Bristol, BS8 1RJ, UK*

ABSTRACT

The Late Cryogenian Warm Interval (LCWI) refers to a non-glacial interval that separates presumed representatives of the Sturtian and Marinoan panglaciations. Its duration is poorly constrained radiometrically and its deposits are relatively poorly known in most geographic regions. This paper aims to constrain the duration, palaeoenvironments and petrogenesis of such deposits in the classic region of NE Spitsbergen, Svalbard. The succession comprises a 200-205 m dolomitic shale (Macdonaldryggen Member, known as E3, of the Elbobreen Formation) overlain by oolitic dolomite Slangen Member (E4), 15-25 m thick, with limestone developed at top and base of E3 in the south of the area. The assumed age context of the succession has been confirmed by the presence of a typical Sturtian cap carbonate profile of negative to positive $\delta^{13}\text{C}$, and primary Sr isotope compositions of basal E3 limestones <0.7072 and of upper E3 limestones of 0.7076 .

At the base of E3, interstratification of cap carbonate with ice-rafted and redeposited glacial sediments occurs. Early diagenetic stabilization of carbonate mineralogy from a precursor, possibly ikaite, to calcite or dolomite is inferred. E3 is predominantly dolomitic silt-shale, with sub-millimetre lamination, lacking sand or current-related sedimentary structures. Thin fine laminae are partly pyritized and interpreted as microbial mats. Dolomite content is 25-50%, with $\delta^{13}\text{C}$ values consistently around $+4\text{‰}$, a value attributed to buffering by dissolution of a precursor metastable carbonate phase. Local calcite cement associates with low $\delta^{13}\text{C}$ values. The carbonates form silt-sized, chemically zoned rhombic crystals from an environment with dynamically changing Fe and Mn. Three-dimensional reconstructions of cm-scale disturbance structures indicate that they represent horizontally directed sock-like folds, developed by release of overpressure into thin surficial sediment overlying an early-cemented layer.

A shoaling upwards unit near the top of E3 displays calcium sulphate pseudomorphs in dolomite in the north, but storm-dominated limestones in the south, both being overlain by peritidal oolitic dolomites, exposed under the succeeding Wilsonbreen glacial deposits. There is no Trezona $\delta^{13}\text{C}$ anomaly, possibly implying top-truncation of the succession.

Regular 0.5 m-scale sedimentary rhythms, reflecting subtle variations in sediment texture or composition occur throughout E3 and are interpreted as allocyclic. They are thought to be mainly primary in origin, locally modified slightly during early diagenetic cementation. Rhythms are proposed to represent ca. 18 kyr precession cycles, implying 6-8 Myr deposition between glaciations.

¹ Corresponding author at School of Geography, Earth and Environmental Sciences, University of Birmingham B15 2TT, UK. Tel: +441214144181. E-mail address: i.j.fairchild@bham.ac.uk (I.J.Fairchild)

Keywords:

Cryogenian

shale

rhythmic sedimentation

chemostratigraphy

orbital forcing

dolomite

1. Introduction

Distinct and widespread glaciation is a key phenomenon of the Earth system in the Cryogenian Period (Fairchild and Kennedy, 2007; Shields-Zhou et al., 2012), but much less attention has been paid to the non-glacial deposits. Recent radiometric dates have strengthened the view of two widespread glaciations, one starting near the beginning of the Cryogenian (redefined to be 720 Ma, IUGS, 2014), and one finishing at the Cryogenian-Ediacaran boundary (Rooney et al., 2015). The intervening period is referred to as the Late Cryogenian Warm Interval (LCWI) by Shields et al. (2012). Based on new observations from Svalbard, we determine the palaeoenvironments and petrogenesis of the shale-dominated LCWI, place constraints on its duration from cyclostratigraphy, and assess its chemostratigraphic correlations.

The 720 Ma lower Cryogenian boundary is close to a cluster of precise U-Pb dates on zircons recording the onset of glaciation in NW Canada (716–717 Ma, Macdonald et al. 2010), Oman (711 Ma, Bowring et al., 2007) and South China (716 Ma, Lan et al., 2014). Likewise, the basal, globally correlated cap carbonate to the Marinoan glaciation, which defines the Cryogenian-Ediacaran boundary, is well-constrained to ca. 635 Ma based on radiometric ages in China (Condon et al., 2005; Zhang et al., 2008), Namibia (Hoffmann et al., 2004), Tasmania (Calver et al., 2013) and NW Canada (Re-Os date; Rooney et al., 2015). Both early and late Cryogenian glaciations, referred to as the Sturtian and Marinoan (based on locations in South Australia), respectively, appear to be globally distributed (Li et al., 2013). In some regions, the history of one or both glaciations is locally or regionally complex, with distinct glacial retreat intervals recognized in South Australia (Williams et al., 2008, Le Heron et al., 2011; Rose et al., 2013), Namibia (Hoffman, 2011; Le Heron et al., 2013), Scotland (Spencer, 1971; Arnaud and Fairchild, 2011) and Oman (Leather et al., 2002; Rieu et al., 2007a). However, semi-continuous Cryogenian successions display a clear stratigraphic motif in which two glacial units bound an unambiguously non-glacial interval, representing a mid-Cryogenian interlude of unknown duration (~5–27 My; Rooney et al., 2014). The Neoproterozoic succession of NE Svalbard, formerly contiguous with present-day Northeast Greenland (formerly known as East Greenland; Knoll et al., 1986; Fairchild & Hambrey, 1995; Hoffman et al., 2012), preserves this Cryogenian non-glacial interval.

Chronological and chemostratigraphic constraints on the mid-Cryogenian in general, although improving (Halverson et al., 2010; Rooney et al., 2014, 2015), are currently more fluid than the base and top of the Cryogenian (Spence et al., 2016). A tuffaceous bed just above the Sturtian glaciation in South China has yielded a U-Pb age of 663 ± 4 Ma (Zhou et al., 2004). Re-Os dates from Sturtian gap carbonates have yielded dates of 662.4 ± 4.6 Ma (NW Canada, Rooney et al., 2014), 659.0 ± 4.5 Ma (Mongolia, Rooney et al., 2015) and 657 ± 7 (Amadeus Basin, Australia, Kendall et al., 2006). Arguments to disregard rather younger dates from the Adelaide rift basin (Kendall et al., 2006, 2009) were presented by Rooney et al. (2014). Dates for the onset of Marinoan glaciation are less constrained. U-Pb ages of 654.5 ± 3.8 Ma and 636.3 ± 4.9 Ma from tuffs immediately below the Nantuo Formation, and within the Nantuo Formation in South China (Zhang et al., 2008) respectively, provide the tightest age constraints on the onset of Marinoan glaciation. In summary, current knowledge from radiometric dating suggests the mid-Cryogenian glacial interval represents the time between c. 663–659 Ma and c. 654–636 Ma, a duration of between 5 and 27 My.

Salient chemostratigraphic features of the interval between glaciations include: 1) a rise and fall in weathering-controlled chemical index of alteration (CIA; Rieu et al., 2007b); 2) high $\delta^{34}\text{S}$ values in sedimentary pyrites and carbonate-associated sulphate (Gorjan et al., 2000; Hurtgen et al., 2002; Li et al., 2012); 3) initially strongly rising, then slightly rising $^{87}\text{Sr}/^{86}\text{Sr}$ pattern (Halverson et al., 2007); 4) a basal negative $\delta^{13}\text{C}_{\text{carbonate}}$ anomaly (Sturtian cap carbonate), followed by heavy carbonate $\delta^{13}\text{C}$ signatures punctuated by the pre-glacial, deep negative Trezona anomaly (Halverson et al., 2002), and possibly an older (Tayshir) anomaly, as seen in the lower Tsagaan Oloom Formation in SW Mongolia (Macdonald et al., 2009). Detailed palaeoenvironmental interpretations of the mid-Cryogenian are patchy. The most comprehensive studies have been performed on thick carbonate successions in South Australia (e.g. McKirdy et al., 2001; Giddings and Wallace 2009a, b; Rose et al., 2012; Hood & Wallace, 2014, 2015; Wallace et al., 2015) and Namibia (Halverson et al., 2002, 2005, 2007; Hoffman and Schrag, 2002; Hurtgen et al., 2002; Hoffman and Halverson, 2008; Hoffman, 2011), and mixed carbonate-siliciclastic sediments of NW Canada (Hofmann et al., 1990; Narbonne and Aitken, 1995; Day et al., 2004).

NE Svalbard presents two Cryogenian glacial units, presumed to be Sturtian and Marinoan equivalents. The intervening mid-Cryogenian non-glacial interval is exposed on the mainland (NE Spitsbergen) and on

Nordautlandet (Fairchild & Hambrey, 1984; Halverson et al., 2004; Hoffman et al., 2012; Riedman et al., 2014; Tahata et al., 2015; Kunzmann et al., 2015). The strata are steeply dipping, but unmetamorphosed and detailed geological maps are given in Hoffman et al. (2012) and Fleming (2014, p. 121-122). We re-describe and test the correlations of the well-exposed Spitsbergen outcrops (Figs. 1 and 2), primarily using Sr and C isotope chemostratigraphy, and new evidence is presented for the presence of a Sturtian cap carbonate. It is argued that previously undescribed regular sedimentary rhythms appear to be orbitally controlled, allowing an estimate to be made of the minimum duration of the non-glacial interval. The rhythms are found within a remarkably uniform dolomitic shale facies which is shown to display evidence for early cementation in an environment subject to dynamic variations in Fe and Mn, and yet unlike Phanerozoic ferruginous carbonates, maintains positive $\delta^{13}\text{C}$ values. This study contributes to understanding of the non-glacial Cryogenian and the under-researched field of Neoproterozoic shale sedimentology. It also points to the potential importance of cyclic shale units in the Proterozoic.

2. Methods

2.1 Field, magnetic susceptibility, petrographic and reconstructive methods

Field sections were measured by tape and Abney level and corrected to true thickness, or directly measured in cliffs; total thickness was checked by GPS. Samples were taken, primarily for chemical analysis at a minimum interval of 5 m and sawn in half. Around 40 samples were studied in polished or stained thin sections. Polished sections were studied by cold-cathode cathodoluminescence (CL) at 15 kV and several of these also by backscattered electron microscopy (BSE) on a Phillips XL30 environmental SEM operated at 15 kV and combined with qualitative elemental analysis. One 6 m field section was sampled completely at 2 cm resolution (three hundred 10 g samples). A sub-set (120) of this intensive sample set were ground to a fine powder and measurements made in triplicate of total magnetic susceptibility in a KLY-3S Kappabridge instrument (supplementary Table S1).

Two computer-generated three-dimensional reconstructions of centimetre-scale structures in dolomitic shales were made from serial sections. Sawn rock surfaces were flattened and serially ground on a rotating lab covered with a plate coated with 40 μm diamond paste, checking the amount removed (to the nearest 0.1 mm) with vernier calipers. Each fresh surface was photographed wet in a fixed position and the SPIERS (Serial Palaeontological Image Editing and Rendering System) software suite (Sutton et al., 2012) was used to align the images and build a 3-dimensional template, with the aid of repeated manual adjustment of contrast and brightness to specify sedimentary laminae.

2.2 U-Pb dating of detrital zircons

Zircon grains from four pre-glacial samples (member E1) were processed and separated using standard gravimetric and magnetic separation techniques at the NERC Isotope Geoscience Laboratories (UK). Zircon grains (standard and unknowns) were emplaced in epoxy mounts and polished to expose the grains. Photomicrographs and CL images were used to characterize the internal structures of each grain to allow unzoned samples to be selected, and to help recording laser spot locations. The laser study was performed using a New Wave Research solid-state Nd:YAG laser ablation system coupled with a HR-Nu instrument ICP-MS in the NIGL laboratories. A further sample from the Wilsonbreen Formation was analyzed at the University of Adelaide using similar techniques in which analysis was carried out using an Agilent 7500cs ICPMS coupled with a New Wave 213 nm Nd-YAG laser. Further details of methods are given in laboratories Roberts et al. (2011) and data are listed in Supplementary Table S4.

2.3 Sr isotope analysis

For determination of $^{87}\text{Sr}/^{86}\text{Sr}$, 40-60 mg of sample powder was weighed, and then leached with 0.5 M HCl for 24 hours at laboratory temperature. Samples were then centrifuged, acid pipetted out and dried at 110°C. Sr was separated from the matrix using pre-cleaned Eichrom Sr spec resin. Approximately 150 μL of resin was loaded into a pre-cleaned and fritted 1 mL pipette tip. The samples were loaded onto a cleaned and conditioned resin in 1 mL of 2M HNO_3 . The samples were then washed with 0.4 mL of the same acid, 1 mL of 7 M HNO_3 and 0.2 mL of 2M HNO_3 . The Sr cut was then collected in 1 mL 0.05 M HNO_3 and dried. Total procedure blank is negligible (~ 20 pg) relative to the amount of Sr processed through the column (~ 500 ng). The total yield was close to 90%.

Sr isotopes were analysed at the Open University using the ThermoFisher Triton TIMS. The samples were loaded onto degassed Re filament following the procedure described by Charlier et al. (2006). Sample filaments were heated to $\sim 1460^\circ\text{C}$ and the Sr beam was tuned to obtain a stable signal of ~ 8 V of ^{88}Sr . Raw Sr isotopes ratios were corrected for instrumental mass fractionation using the exponential law and a $^{86}\text{Sr}/^{88}\text{Sr}$ ratio of 0.1194. In this study, each measurement consists of collecting 240 ratios in 24 blocks of 10 cycles, with each ratio representing 8.4 seconds of integration time. A baseline is measured and the amplifiers are rotated after each block. An internal precision of ~ 10 ppm (2 s.e.) was obtained and the external repeatability was assessed by multiple analysis of a standard (NIST 987) and is equal to ~ 15 ppm (2 s.d., $n = 5$). The NIST 987 $^{87}\text{Sr}/^{86}\text{Sr}$ ratio measured in this study is 0.710224 ± 0.000011 . Data are listed in Supplementary Table S1.

2.4 Elemental analysis (Supplementary Tables S1 to S3)

Samples for ICP-AES analysis at Royal Holloway were prepared by drilling 4 mg of sample powder from fresh, sawn surfaces covering with 2 mL of 1.6 M (10% v/v) Aristar-grade HNO_3 and allowing to react overnight at laboratory temperature, before dilution to 0.3 M and removal from insoluble residue. The acid strength was relatively high to optimize dissolution of ferroan carbonate phases. Analyses were corrected using three standards matrix-matched for limestones and similarly for dolomites. Ca, Mg, Fe and Mn analyses were converted to equivalent mass carbonate to derive an analytical total from which the insoluble residue was derived by difference. Elemental concentrations were then calculated for these elements (together with trace elements Sr, Ba and Zn) assuming them to lie in the carbonate fraction. Repeat analyses from new dissolutions normally lie within 5 %.

X-ray fluorescence (XRF) analysis on 40 consecutive samples from the intensively sampled suite mentioned above was carried out at the University of Leicester on a PANalytical Axios spectrometer using fused glass beads prepared from dried powders in a ratio of 1:5 with 100% Li tetraborate flux. Elements determined were Si, Ti, Al, Fe, Mn, Mg, Ca, Na, K, P and S, together with loss on ignition; data are presented conventionally as oxides and analytical totals were 99.7 ± 0.9 %.

Microanalysis was carried out at the Edinburgh Ion Microprobe Facility on a Cameca 4f instrument on polished, gold coated thin sections using a primary O⁻ beam to generate positive secondary ions. A beam current of 0.5 nA was used. The beam was focused to an analytical area of $c.2 \mu\text{m}$ with an overall diameter of 5-7 μm . An offset of 75 kV was used with a vertical step size of 5 μm . Ions of ^{24}Mg , ^{27}Al , ^{30}Si , ^{42}Ca , ^{54}Fe , ^{55}Mn , ^{88}Sr , ^{89}Y , ^{138}Ba and ^{140}Ce were counted. Results were standardised using internal standards Oka Carbonatite and Norman Cross Calcite.

For CO_2 (carbonate carbon) analysis at by Activation Laboratories Limited (Ontario), powdered sample (0.2 g) was thermally decomposed at 1000 °C, H_2O removed in a moisture trap, and CO_2 determined by an infra-red cell. Organic carbon analyses were determined at the same laboratories using the difference between total carbon and carbonate carbon, but most values were below the effective limit of determination of 0.2 wt. % and are not reproducible.

2.5 Carbon and oxygen isotope analysis

Carbon and oxygen stable isotope data are presented here as $\delta^{13}\text{C}$ and $\delta^{18}\text{O}$ in parts per thousand with respect to the VPDB standard. Data are listed in supplementary table 1 and include analyses from Fairchild & Spiro (1987) and Halverson et al. (2004). New data was obtained at the University of Birmingham using a

continuous-flow Isoprime IRMS, with a multiflow preparation system. Samples of between 80-250 μg powdered carbonate were reacted with phosphoric acid at 90°C for at least 90 minutes; results were calibrated using IAEA standards NBS-18 and NBS-19 and repeatability on an internal standard was better than 0.1‰ for $\delta^{13}\text{C}$ and 0.15‰ for $\delta^{18}\text{O}$. Data are reported in Supplementary data Table S1.

3. Lithostratigraphy and correlations

Cryogenian sediments in Svalbard occur within the Polarisbreen Group of the Hekla Hoek Supergroup and comprise the Elbobreen, Wilsonbreen and Dracoisen formations, subdivided into members, which are abbreviated by means of numbers (Table 1; Hambrey, 1982). An earlier glaciation (member E2) is correlated with the older Cryogenian (Sturtian) glaciation (Halverson et al., 2011), and a later glaciation (Wilsonbreen Formation) is truncated by a transgressive succession correlated with the basal Ediacaran (Halverson et al., 2004), substantiating a Marinoan age. The intervening non-glacial interval was interpreted by Fairchild & Hambrey (1984) as a single shoaling-upwards sequence to represent offshore marine dolomitic shales (member E3) shallowing upwards to a dolomitic ooidal grainstone with anhydrite pseudomorphs and peritidal tepee structures (member E4) deposited in a restricted, shallow, warm environment. The upper boundary of E4 is a subaerial exposure surface with evidence for frost-wedging.

Halverson et al. (2004) proposed an alternative model in which E2 to E4 and the Wilsonbreen Formation were deposited within a single (Marinoan) glaciation. This accounted for: a) the presence of a negative carbon isotope anomaly (correlated with the sub-Marinoan Trezona anomaly) beneath E2, but not beneath the Wilsonbreen Formation, despite no evidence of significant truncation at that surface, b) the lack of a clear stratigraphic $\delta^{13}\text{C}$ profile akin to other sequences in this non-glacial time interval, and c) the presence of pseudomorphs within E3, interpreted as glendonites (after ikaite). In this model, the uniformly fine-grained E3 facies were interpreted to have been deposited beneath permanent ice cover. The later discovery of a carbon isotope anomaly (the Islay anomaly) beneath Sturtian-aged sediments elsewhere, along with new strontium isotope data from the Russøya (E1) member tipped the balance of evidence back to the two-glaciation model (Halverson, 2006; Halverson et al., 2007).

Riedman et al. (2014) found only depauperate acritarch assemblages in E3, dominated by simple spheres, but found such low diversity assemblages to be typical also of the Sturtian and post-Sturtian interval in Australian sections. Tahata et al. (2015) carried out a microanalytical Fe-isotope study of pyrite in Polarisbreen Group sections in Nordaustlandet to the NE of our study area and observed $\delta^{56/54}\text{Fe}$ in E3 up to $+3.91 \pm 0.29\text{‰}$, indicative of iron oxidation at a chemocline above a ferruginous ocean. They also presented low-resolution $\delta^{13}\text{C}$ data which are consistent with those presented herein. The iron-speciation and trace metal study of Kunzmann et al. (2015) which includes some E3 samples, likewise confirms an anoxic, ferruginous ocean.

We have re-measured two nearly complete sections originally presented by Fairchild & Hambrey (1984) at Dracoisen and Ditlovtoppen (Fig. 2). A new location in SE Andromedafjellet, informally termed Reinsryggen, presents a continuous section, but is much thinner because of strata cut out by a fault crossing the section just below the E3-E4 boundary. Despite this, the top of E3 and all of E4 are exposed here, as they are in several incomplete sections to the south (Halverson et al., 2004). We present a new, field-excavated section of the base of E3 from the south Backlundtoppen location and in upper E3 from the north Backlundtoppen ridge (Fig. 2). Both of these sections contain limestones from which useful new Sr isotope data were obtained.

4. Sedimentology, diagenesis and environmental evolution

4.1 The E2-E3 transition

Introduction

Fairchild & Hambrey (1984) described and interpreted diamictite and rhythmite facies of E2, recording a consistently sharp boundary to dolomitic shale at the base of E3. However, Halverson et al. (2004) additionally recorded a transitional contact between glaciogenic facies in E2 and laminated limestones at the South Backlundtoppen section. The key issue here is whether distinctive features of a Sturtian cap carbonate (Kaufman et al., 1997; Kennedy et al., 1998) are present.

Description

E2 is typically 10-15 m thick and near its top is dominated by sharp-based conglomerates, graded silty-sandstones with climbing ripples and dropstones, and millimetre to centimetre-scale clastic rhythmites (e.g. Fig. 3A, B). The boundary between the top of E2 to laminated shaly carbonates of Member E3 is sharp except in the South Backlundtoppen section (Fig. 2) where a 30 cm interval of limestone rhythmites occurs a metre below the top of E2 (Fig. 3B), exhibiting within-layer asymmetric folds and thrusts (Fig. 3D). Observed petrographically, these rhythmites consist of calcite microspar and are separated by dolomicrite laminae containing sand and silt-grade dolomite and siliciclastic detritus (Fig. 3E). They are overlain by a sharp-based 1.2 m-thick unit varying laterally from conglomerate (Fig. 3B) to silt-to-sand-grade clastic dolomite and in turn by 0.2 m of millimetre-laminated rhythmites with small dropstones (recognized using criteria in Fairchild & Hambrey, 1984). The basal few centimetres of E3 at South Backlundtoppen (Fig. 3C) and Ditlovtoppen (Fig. 3F) consist of dololaminates with significant detritus, dropstones and diamictite pellets. Accessory fine-grained pyrite is nearly ubiquitous in all lithologies. Cathodoluminescence microscopy demonstrates the presence of an authigenic dolomite phase with a bright luminescence zone that surrounds detrital particles which have variable cathodoluminescence characteristics (Fig. 3G, H). Fairchild and Hambrey (1984) found that authigenic matrix dolomite with negative $\delta^{13}\text{C}$ (-1 to -4‰) and high Fe content (>25000 ppm) was characteristic of E2, surrounding clasts with positive $\delta^{13}\text{C}$.

Halverson et al. (2004) recorded laminated limestone with highly variable negative $\delta^{13}\text{C}$ signatures (-3 to -16‰) in the basal metre of E3, probably equivalent to limestone starting at the +1 m level in this study. This limestone has 0.2-0.3 mm-thick microspar laminae with thin intervening micrite laminae and is locally affected by stylolitization (Fig. 4B). The microspar layers locally have millimetre-wide, shallow upward convexities that may reflect an original primary upward mineral growth (Fig. 4C). However, cathodoluminescence demonstrates a distinctive replacive fabric of zoned calcite rhombs (Fig. 4D). Above the +5 m level, the carbonates are dolomite rather than limestone, but have a similar lamination style.

In the other sections, limestone is absent in the basal E3 sediments, but similar facies composed of dolomite are found instead. A consistent CL zonation of dolomicrite to dolomicrospar replacive mosaics overgrown by dolomite cements demonstrates the early diagenetic origin of this dolomite phase (Fig. 5). Dolomicrospar laminae sometimes show upward convexities similar to the Backlundtoppen limestone laminates described above.

Notable sedimentary structures at various levels in the basal few metres of the Backlundtoppen and Reinsryggen sections are recumbent folds a few mm thick with rounded noses (Fig. 4A, 5A). In fold noses, the carbonate fabric breaks up into "pseudo-allochemical" areas by brecciation of the laminates and these are then overgrown by carbonate cement (Fig. 5B, 5F).

Oxygen and carbon isotope data from the whole of E3 and E4 are plotted in Fig. 6 where the vast majority of the negative $\delta^{13}\text{C}$ values are from the E2-E3 transition. Limestones at the base of E3 cluster around -9‰ and display consistently more negative $\delta^{18}\text{O}$ values than dolomite (mostly -1 to -4‰). This offset is greater than the 3‰ expected from equilibrium precipitation from a fluid of the same $\delta^{18}\text{O}$ composition at the same temperature (Land, 1980). Strontium concentrations in the basal 30 m of E3 range from 514 to 705 ppm for limestones and 84 to 319 ppm for dolostones (supplementary data, Table S1).

Highly variable carbon isotope values from the basal limestone bed (Fig. 7) were interpreted by Halverson et al. (2004) as an indication of early, microbially mediated diagenesis (cf. Irwin et al., 1977). Whilst this is valid, the newly enlarged dataset (Fig. 7) shows that such variability, with limestones tending to be lighter than dolomites, is restricted to the basal 2 m (Fig. 7). Overall in the basal 25 m of E3 in the Backlundtoppen section, a consistent rising trend is seen from around -4 to +3‰, corroborated by isolated samples from other sections, and independent of Fe and siliciclastic content. The basal laminated dolomites

at Reinsryggen have slightly negative $\delta^{13}\text{C}$ values, and it is possible that they are coeval with dolomites in the 5-10 m interval at Backlundtoppen.

Interpretation

Based on the criteria developed by Fairchild & Hambrey (1984), massive diamictites represent the bulk rain-out from a high density of icebergs in a proximal glacial marine position, whereas the lensing beds of matrix-supported breccia represent subaqueous sediment gravity flows (possibly close to the grounding line). Rhythmites reflecting cyclic tidally-influenced sedimentation from sediment plumes emerging from ice cliffs below wave-base (cyclopels and cyclopsams). Glacially derived sediment diminished rapidly at the E2-E3 boundary and sediment particles larger than coarse silt are not found above the basal few decimetres of member E3. Such a rapid change in sediment character is consistent with rapid deglaciation. There is no direct evidence of changes in water depth, although significant sea-level rise would be expected at the close of a glaciation.

The sedimentary deformation found in fine sediments (Fig. 4A) is suggestive of downslope movement with recumbent folds and rounded fold noses resembling small-scale slump folds. However, exposures do not permit measurements to demonstrate a consistent slope-related orientation. In microbial laminites in an equivalent cap carbonate from Namibia, Pruss et al. (2010) documented the occurrence of recumbent folds and spiral roll-up structures which are associated with sedimentary dykes indicative of an origin related to liquefaction caused by fluid escape. However, no such ancillary features occur in the E3 sections. Nevertheless, in both cases the deformation is likely to have been restricted to a surficial (no more than decimetre-thick) unlithified, or weakly lithified layer, reflecting similar early cementation of the layers.

The limestone rhythmites found 1 m below the top of E2 at Backlundtoppen have a microsparry character like those near the base of E3 and their presence implies precipitation of a carbonate phase within the water column or at the sediment surface, probably assisted by the presence of microbes (Bosak and Newman, 2003). The relatively uniform thickness of the carbonate layers (Fig. 3B) might imply an annual origin by comparison with lacustrine laminites of the Wilsonbreen Formation (Fairchild et al., 2016), but the regularity is less marked in thin section (Fig. 3F) where layers commonly display a composite structure. Carbonate varves are common in lacustrine environments in various climatic zones (Lawrence and Hendy, 1985; Shanahan et al., 2008) but are not characteristic of marine environments today despite the lack of a physico-chemical reason why they should not occur. Photosynthesis is more effective in raising carbonate supersaturation in waters of lower ionic strength (Fairchild, 1991), but the depositional waters at E2-E3 boundary times would have been saturated for calcite anyway because of the abundance of detrital dolomite rock flour (Fairchild and Hambrey, 1984). Consequently, seasonal fluctuation in the intensity of photosynthesis is a viable mechanism for their formation. On the other hand, the relatively light oxygen isotope composition of the limestones (-6 to -9‰, Fig. 6) could imply an origin in seawater diluted with meltwater. Limestone layers do not show evidence of physical compaction, implying that the replacement of a precursor by calcite happened during early diagenesis and hence elevated burial temperatures are not required to explain lighter $\delta^{18}\text{O}$ values. The upward convexities are reminiscent of a bulbous mode of upward growth of the precursor from the sediment surface, but there are no preserved inclusions to provide further clues as to the primary style of growth. Less stable calcium carbonate forms that could have been the precursor are amorphous CaCO_3 , ikaite, vaterite or aragonite. Ikaite is an attractive option because it forms preferentially at low temperatures (Shearman & Smith, 1985; Selleck et al., 2007; Oehlerich et al., 2013) such as those expected to coincide with ice-rafting; Fairchild et al. (2016) have shown similar replacive rhombic calcite fabrics to those in basal E3 limestones in replaced ikaite of the Wilsonbreen Formation.

Samples studied from those parts of member E2 close to the boundary with E3 appear texturally to be dominated by detrital dolomite, although an authigenic contribution can be inferred from the negative $\delta^{13}\text{C}$ and signature and high Fe contents (Fairchild and Hambrey, 1984). Authigenic dolomite is visible as a bright CL zone in basal E3 dolomite, although it is mostly dark as expected for a high-Fe phase (Fig. 3H). In E3, dolomite forms laminar carbonates that are texturally very similar to the limestone laminites, and it appears that dolomitization occurs by replacement of a partly lithified precursor phase folded by soft-sediment deformation before compaction and cementation by dolomite (Fig. 5). During the Neoproterozoic, early

dolomitization is ubiquitous in peritidal marine rocks but patchier and in subtidal sediments (Knoll and Swett, 1990). In the case of the E2-E3 boundary sediments, the presence of organic carbon bound to clays and significant sulphate reduction (as evidenced by pyrite content) would have favoured dolomite formation (Mazzullo, 2000; Zhang et al., 2012).

Varying porewater chemistry during diagenetic mineral replacement is implied by the complex cathodoluminescence zonation observed in both calcite and dolomite and the presence of authigenic phases such as pyrite. A localized role for bacterial processes in modifying the $\delta^{13}\text{C}$ of DIC is clear in the basal limestone (Halverson et al., 2004). However, the steady rise in $\delta^{13}\text{C}$ values with stratigraphic height through E3 agrees with a low-resolution study showing an upward rising trend in $\delta^{13}\text{C}$ of both organic carbon and carbonate carbon in the same study area (Kaufman et al., 1997) and implies that the carbon isotope values of E3 carbonates are not dominated by local bacterial influences. The secular rise in $\delta^{13}\text{C}$ occurs in fine-grained post-Sturtian cap carbonates on multiple cratons and implies a global signature (Halverson and Shields-Zhou, 2011), or parallel variations in local conditions such as water depth (Giddings and Wallace, 2009a). The Fe-enrichment and dark colour (up to 0.7 % organic carbon, Kunzmann et al., 2015) are also features of basal E3 which bear comparison with other Sturtian caps (Kennedy et al., 1998), whilst features that are restricted to Marinoan caps (e.g. barite, tepees, giant wave ripples) are absent.

4.2 Dolomitic shale sedimentation in E3

Introduction

Most of member E3 is composed of dolomitic silt-shale, with sub-millimetre scale lamination and no traction structures (Fairchild and Hambrey, 1984). Although no overall change in facies is apparent from 20 to 180 m above its base (Figs. 2, 8A), a strikingly regular rhythmic or cyclic mode of sedimentation is revealed on differentially weathered outcrops at Dracoisen (Fig. 8B) and Ditlovtoppen. The more resistant levels within rhythms (cycles) commonly appear on weathered surfaces to be purer carbonates (Fig. 8C), and locally display a concretionary form in which layer thickness is double that outside the concretion (Fig. 8F). However, more commonly, resistant and non-resistant weathered parts of sedimentary rhythms are more difficult to distinguish close-up (Fig. 8D, E) than at a distance (Fig. 8B) and this subtlety provides a significant challenge. We build up the story through successively describing and interpreting: 1) overall lithology, 2) characteristic sedimentary disturbance structures, 3) petrology and geochemistry and 4) rhythmicity.

Lithology

The siliciclastic component of E3 is dominated by fine to coarse quartzo-feldspathic silt; sand is virtually absent. Typical laminae are 0.1-0.4 mm thick and consist of a thicker, dolomitic silt sub-lamina and a thinner parting, richer in phyllosilicates, often with enhanced levels of framboidal pyrite (Fig. 9A, B, D-G). The silty sub-laminae are locally micro-nodular in character (Fig. 9A), and at certain horizons the laminar structure displays laterally impersistent centimetre-scale disturbances with tightly folded laminae (Fig. 9B, F) which are described in the next section. Above 170 m stratigraphic height, finer laminae are less noticeable (Fig. 9H) and hydrodynamic sediment sorting is shown texturally above 180 m when 100-200 μm -thick lenses of sorted silt and faint cross-lamination appear in what are now dolomitic siltstones rather than silt-shales (Fig. 9C).

The uniform, fine-grained lithology of the main part of member E3, coupled with evidence for consistent sub-millimetre scale lamination indicates a regime of slow sedimentation without strong hydrodynamic activity. In particular, sharp-based or graded units are absent and laminae are more continuous than the lensing structures that can form in shales from redeposition of soft mud clasts (Schieber et al., 2010). The implied depositional environment was consistently below wave base until the first signs of sorting in lensing laminae (e.g. Fig. 9C) near the top of the member. The lack of evidence for sediment gravity flows implies a continental shelf, rather than slope environment, and hence water depths of the order of 100-300 m. The presence of laminae varying in grain size indicates some variation in sediment supply and accumulation.

Pale, micronodular laminae imply early carbonate cementation, and these layers would have resisted compaction. The discrete, thin, and flexible nature of the finer, darker laminae is consistent with an origin as

microbial mats, which are well-known in Proterozoic offshore siliciclastic sediment (Schieber, 1986). Such mats typically metabolized by anoxic photosynthesis. The focussing of organic matter in these horizons is consistent with the preferential occurrence of pyrite (Schieber, 1986; Pruss et al., 2010).

Disturbance structures

Field and petrographic observations show that the deformed laminae noted above (Fig. 9B, F) form a distinct geometric class of sedimentary structure, referred to here as disturbance structures, which have similar characteristics throughout the main part of member E3. These structures are visible in the field in discrete horizons (Fig. 2), although require optimal weathering and illumination to be clearly seen. The structures form equant, centimetre-scale concave or convex markings (Fig. 10A) with curved and upturned laminae (Fig. 10B). Locally they form trains of several structures with up to centimetre-scale separation (Fig. 10C). In transverse section, structures exhibit a core of concentric ovoid laminae with lamina disturbance decreasing away from the structure; hence they are stratigraphically confined on a centimetre-scale (Fig. 10D) and hence are much smaller than the structures interpreted above as slump folds from the base of member E3. Locally they form more complex en-echelon arrays in which apparently continuous, but deformed laminae separate each structure (Fig. 10E).

A three-dimensional model was constructed from the sample shown in Fig. 10F from 71 serial sections cut to a depth of 9 mm. The model shows the concentric core laminae (Fig. 10G) to be conical, flaring into the sectioned slab (upwards in Fig. 10H, I). The terminations are complex (e.g. double-pointed in Fig. 10H) and the flattened nature of the cones indicates an overall sheath-like geometry. The core is surrounded by continuous laminae (e.g. green layer in Fig. 10J), then by disturbed laminae (purple and blue, Fig. 10J), the deformation of which is disjointed from the inner part of the structure.

A second model was generated from the lower right of the slab shown in Fig. 11A based on from 31 sections cut to a depth of 6.2 mm. This model reveals an en-echelon train of structures, each with a tubular core that is ovoid in cross-section (Fig. 11B) and narrows into the slab (Fig. 11C). The lamination separating some of the structures is clearly continuous (e.g. Fig. 10A), but laminae are bent in such a way as to suggest a reverse fault geometry. Otherwise, laminae more than a few millimetres above a disturbance structure appear to be unaffected. A deeper serial section cut through this sample reveals brittle deformational structures, e.g. the sharp apparently reverse-fault offset arrowed in Fig. 10D which appears to continue as a normal fault lower in the slab.

In summary, the typical geometry of the E3 structures can be summarized as horizontally directed prolapses— that is, sheath-like folds flattened in the horizontal plane. In plan view, the direction of movement is unclear as the structures are equant and internal lamination is only locally visible, but the direction of closure of lamination can be discerned by serial sectioning. The available evidence indicates no preferred orientation of the structures.

We can rule several possible origins for these structures on geometric grounds. The unbroken lamination rules out an origin as trace fossils, whilst the only putative body fossil that shows similarities is *Horodyskia*, which manifests as a chain of bead-like structures (cf. Fig. 10C) but is preserved as pits or moulds (Grey et al., 2010), lacking internal lamination. Likewise, the sheath-like cores to the E3 structures are laminated throughout, unlike the sediment packing of animal burrows. Also, the structures differ from the family of microbial mat-related phenomena known as “wrinkle structures” (Porada & Bouougri, 2007) because the E3 structures are irregularly spaced, rather than forming a continuous, self-organized network.

The closest similarity in external morphology is with horizontal tubular structures termed roll-up structures which are found in modern coastal environments, and both shallow and deep Proterozoic laminated sediments (Sarkar et al., 2014). There are two Proterozoic examples described in detail. Simonson and Carney (1999) described centimetre-high and up to decimetre-wide recumbent folds with rounded limbs and inconsistent vergence within partially carbonate-cemented shales of the Palaeoproterozoic Hamersley Group of Western Australia. Pruss et al. (2010) illustrated a variety of fold structures up to 10 cm wide by 1 cm wide, and commonly containing spiral laminae, found associated with sedimentary dykes in thinly laminated microbial laminites of Sturtian cap carbonates of Namibia. In modern coastal environments rollups form where a microbial mat breaks and edges curl up due to subaerial exposure (Sarkar et al., 2014), whereas the ancient deep-water structures are less completely understood.

Although E3 disturbance structures do not contain spiralling laminae and hence they cannot be termed rollup structures, a comparison is still instructive. The first point is that roll-up structures demonstrate sediment elasticity, a property which arises from the abundance of mucilaginous extracellular polymeric substances (Beraldi-Campesi & Garcia-Pichel, 2011; Chew et al., 2014). The lack of breakage of layers, despite tight bending, is seen too in the E3 disturbance structures, and they are also interpreted to contain mats.

The second point of comparison with rollup structures is the trigger for deformation. In their Hamersley example Simonson & Carney (1999) could not decide between several candidate triggering mechanisms: downslope movement, current shear, high pore-fluid pressures and cyclic disturbance by seismic waves. However, in the Rasthof examples, the associated dykes appear to have been zones of active fluid escape at the time of sedimentation, and Pruss et al. (2010) interpret the roll-up structures to be associated with local liquefaction related to dyke emplacement.

The E3 disturbance structures, occur throughout the affected sediments, rather than being focused at specific event horizons, and do not have a preferred orientation. Hence, there is no direct evidence for current shear, seismic disturbance or downslope movement, but the very small scale of the disturbances is consistent with localized deformation triggered by excess pore pressure in liquefied sediment. A key point is that the structures are not strongly compacted and hence subsequent, near-surface cementation can be inferred (as in the case of Simonson & Carney, 1999). This is also consistent with the presence of undisturbed lamination a few millimetres above disturbance structures. Hence, the deformation is associated with a surficial layer, capable of ductile deformation, as would be a strong and elastic mat, overlying progressively more rigid, cemented sediment. If early cementation was focused more in some laminae than others, pore fluid pressures would be raised beneath more lithified horizons, as physical compaction proceeds. In E3, evidence of localized fracturing of slightly cemented layers (Fig. 11D) is consistent with release of underlying fluid. Rather than forming dykes as in the Rasthof Formation (Pruss et al., 2010), the pore fluids in E3 sediments appears to have been a locally erupted into a less cemented, lower pressure layer propelling a small clot of sediment sideways, creating the prolapsed structures. The en-echelon structure can be interpreted as an oblique fault zone within which fluid is released, either on several distinct occasions, or more likely simultaneously at several different levels within the 1.5 cm-high structure, with little deformation at intervening slightly more cemented horizons (e.g. 2 on Fig. 11A).

It can be predicted that such small-scale fluid-escape structures, which are difficult to study in the field, may be much more widespread in Neoproterozoic shales than have been described up to now. As has been shown, they provide useful evidence for the nature of early diagenesis.

Geochemistry and petrology

The stratigraphic variation of $\delta^{13}\text{C}$ in the 20-180 m interval is extremely limited, with dolomite values nearly all in the range of +2.5 to +4‰ (Fig. 12). Low, outlying $\delta^{13}\text{C}$ values almost all contain significant calcite and hence we infer that the calcite has a lower $\delta^{13}\text{C}$ value than dolomite in the same samples. The calcitic samples also have lower insoluble residue contents (Fig. 13). Dolomites show more variation in $\delta^{18}\text{O}$ (4‰) than $\delta^{13}\text{C}$ (2‰, Figs. 7, 12), and there is a clear upward stratigraphic trend in $\delta^{18}\text{O}$ from 40-180 m in both Dracoisen and Ditlovtoppen. However in the 20-40 m interval, $\delta^{18}\text{O}$ varies from -6 to slightly above 0‰ and varies between sections. The only other measured parameter showing a stratigraphic trend is acid-soluble Fe (plotted as FeCO_3), which diminishes upwards (Fig. 13), and is slightly higher in Ditlovtoppen samples than at Dracoisen.

The mineral textures and internal structures are most clearly revealed in CL and BSE microscopy (Fig. 14). Dolomite forms chemically zoned crystals (Fig. 14A, B, E) of similar size to the siliciclastic silt. The zones are rhombic, but the external crystal shape is subhedral, adjacent to silicates, or anhedral against other dolomite crystals (Fig. 14E, F). Calcite shows less regular crystal shapes (Fig. 14E) and tends to occur more discretely as larger irregular crystals (Fig. 14F). In the concretion of Fig. 8F, calcite crystals enclose detritus and dolomite crystals alike (Fig. 14D) and hence post-dates dolomite.

Ion microprobe microanalysis reveals that most individual crystals display zonation as illustrated for one of the samples in Fig. 15A. Individual crystals either show Fe-Mn covariation or variation in Fe alone. Strikingly, both dolomite and calcite show the same overall range in concentration, and this pattern is found

in other samples. Overall Fe-Mn covariance is shown by crystal means (Fig. 15B) with up to two orders of magnitude variation in Fe and three in Mn. This extraordinary heterogeneity is reflected in the CL characteristics of the carbonates (Fig. 14A-C) where no common pattern of zonation is discernable. Comparison of ICP and ion probe analyses illustrates that although Mn analyses are closely comparable, bulk acid-soluble Fe is close to the maximum observed for means of crystals analyzed by ion microprobe (Fig. 15B) and hence that the acid attack is releasing Fe from other phases as well as carbonate.

The presence of micronodular laminae (Fig. 9A), macroscopic uncompacted concretions (Fig. 8F) and sediment disturbance structures all point to the role of early cementation by dolomite. Calcite post-dates dolomite petrographically and the low insoluble residue of calcitic lithologies (Fig. 13) implies that calcite fills remaining porosity at horizons where dolomite cementation was sufficient to resist any further compaction. Calcite and dolomite precipitating from fluids with the same $\delta^{18}\text{O}$ at the same temperature are expected to differ in $\delta^{18}\text{O}$ by 3‰ (Land, 1980), but most calcites have even lower $\delta^{18}\text{O}$, consistent with an origin at higher temperature.

Both calcite and dolomite scavenge Fe^{2+} and Mn^{2+} from solution during growth (Veizer, 1993; Rimstidt et al., 1998) and so their highly variable Fe-Mn chemistry (Fig. 15) can be assumed to be a direct reflection of the changing pore fluid composition of these elements. Changing availability of Fe and Mn either reflects microbial reduction of progressively more refractory oxidized sources of these minerals (Irwin et al., 1977) or downward diffusion from overlying seawater with fluctuating Fe-Mn chemistry. The lack of $\delta^{13}\text{C}$ variability in dolomites implies buffering by a pre-existing fine-grained carbonate phase. Since CL zonation shows that crystals grew at different times, the precursor is likely to have dissolved progressively, permitting the sustained gradual precipitation of dolomite. The precursor then presumably become exhausted by the time that calcite precipitated, leading to a lower $\delta^{13}\text{C}$ value indicative of a partial source of carbon from breakdown of organic matter (Mozley and Burns, 1993). Conversely, the consistent $\delta^{13}\text{C}$ signature of the dolomites can be used for chemostratigraphic purposes as an indicator of marine water $\delta^{13}\text{C}$ values. This result is unexpected, given the hypothesis that light $\delta^{13}\text{C}$ values would characterize authigenic carbonate in deeper marine settings (Schrage et al., 2013), but is consistent with the low organic carbon content of the sediments (Kunzmann et al., 2015 record values <0.3 %).

The up-section reduction in acid-soluble Fe (Fig. 13), which coincides with a rise in organic carbon to values of 0.5-1 % (Kunzmann et al., 2015), may reflect changes in both carbonate and silicate fractions and this is being investigated in a separate study of clay mineralogy and Fe-speciation. If the up-section 3‰ increase in $\delta^{18}\text{O}$ of dolomites (Fig. 12) were caused simply by changing temperature of formation, it would imply a decrease of >12°C, which is unlikely given the otherwise consistent character of the sediments. Other studies have shown oxygen isotope compositions of early diagenetic carbonate concretions to be more negative than expected at equilibrium (Mozley and Burns, 1993) and that this is markedly so for siderites precipitated from microbial rather than inorganic systems (Mortimer and Coleman, 1997). Hence, kinetic effects linked to varying availability of Fe are interpreted to be responsible for the $\delta^{18}\text{O}$ trend.

Rhythmicity

The rhythmic bedding in E3 shows up prominently in certain field photographs (Fig. 8), but it is difficult to quantify. We have accurately logged the stratigraphic position of the centre of each of the more resistant horizons which define each cycle, but thickness measurements of these horizons are imprecise since these beds usually do not have sharp bases or tops. Time permitted logging of only one profile each at Dracöisen and Ditlovtoppen; comparable cycles to those found at these two localities were only locally visible at Reinsryggen and Backlundtoppen.

The Ditlovtoppen section presents the greatest number of cycles: 270 are visible in the 12 m to 195 m interval above the base of E3 (Fig. 2). The histogram of thicknesses presents a mode in the range 0.4-0.6 m and a positive skew (Fig. 16C). Overall, the cumulative thickness plot is fairly linear (Fig. 16A), but with discontinuities at stratigraphic heights of around 50, 80 and 150 m (above the base of E2), where unusually thick rhythms are present. Lack of clear exposure of some rhythms presents a ready explanation for the positive skew of the thickness histogram (Fig. 16C) and the mode is taken as more representative of their true thickness.

The Dracoisen section presents 120 cycles between the 45 m and 170 m level in the section, with no stratigraphic trends (Fig. 16A) and with a higher mean value and a stronger skew than at Ditlovtoppen (Fig. 16B, C). The Dracoisen section was logged in the upper centre of Fig. 8B, but the photograph illustrates that many cycles visible in the cliff in the foreground become less clear laterally. Also, since the total thickness of E3 is virtually identical at both sections and they are only 10 km apart, the data from Dracoisen are regarded as less complete. The modal thickness, between 0.8 and 1.2 m, is likely to contain a significant proportion of double rhythms, and the tail of the distribution likely includes multiple rhythms. The Ditlovtoppen histogram (Fig. 16C), with a mode at around 0.5 m, is regarded as being closer to the true picture.

Since field observations were necessarily imprecise, laboratory data was used to specify the lithological nature of rhythms based on a combination of geochemical analyses and magnetic susceptibility (MS) measurements. Samples were taken from representative resistant/less resistant lithologies throughout E3 and on selected samples from a high resolution suite of 300 collected between 40 and 45 m height in the Dracoisen section and covering seven cycles. Organic carbon content could not be used since most samples were below detection limits (0.2 wt. %) for total organic carbon.

Since the ratio of carbonate to siliciclastic sediment is the commonest mode of variability in offshore cyclic sediments (Ricken, 1986, 1996), plots of CaCO_3 content of total sediment were generated (Fig. 17C, D). Although the basal cycle shows a resistant horizon with high Ca content at 46.5 m, such a correlation is not obvious higher in the intensively sampled section (Fig. 17C), nor is there any clear distinction in Ca content between field-described 'dolomites' and 'dolomitic shales' in the profile as a whole (Fig. 17D).

To confirm whether CaCO_3 content is the most appropriate variable, an objective determination of modes of variability was made using Principal Components Analysis on two datasets: 1) XRF and magnetic susceptibility analyses on 40 samples covering 80 cm of the basal cycle (Fig. 17A) and 2) 68 ICP-AES analyses between 50 and 190 m in stratigraphic height, including 35 of the above 40 samples (Fig. 17B).

For the XRF dataset, the first principal component, accounting for 69% of data variability contrasts carbonate-derived elements (Ca and Mn, together with loss on ignition, i.e. largely CO_2) with silicate components (Al, Si, Na, K, Ti, and acid-insoluble residue derived from a separate aliquot). Magnesium scales largely with the carbonate component and Fe more with the silicate component. Magnetic susceptibility loads with the silicate component but more weakly than the other variables. The second principal component groups Fe and S, corresponding to an independent variation in pyrite content. Calculation of modal analyses indicates that Fe is located in carbonates > silicates >> pyrite. For the ICP-AES dataset (referring to acid-soluble, not total chemistry), the first principal component, accounting for 55% of variation contrasts Ca, Sr and Mn with Fe, Fe/Mn, Mg, Zn and insoluble residue, implying that a proportion of Fe, Mg and Zn is leached from non-carbonate phases during acid leaching. Barium displays independent variation, being the most highly loaded element on the second principal component (Fig. 17B). Minor principal components in both analyses do not show any stratigraphically meaningful variation. In combination, the two sets of analyses indicate that Ca is present nearly entirely in carbonates, and confirms that the Ca content (expressed as CaCO_3) of the total sample should provide an effective variable illustrating compositional change.

Taken as a whole, these observations indicate that the main mode of variation in sediment composition is in terms of variation in the carbonate to silicate ratio, but only locally is there a simple correlation between high carbonate (Ca) content and more resistant beds. In such cases, enhanced early cementation, leading to higher carbonate content, likely created a lithology more resistant to weathering. Otherwise, there must be subtle textural differences between more and less weathering-resistant parts of cycles. The very subtlety of the cycles provides reassurance that they are indeed of primary origin. In Phanerozoic rhythms, it is common to find significant diagenetic enhancement of primary differences in carbonate content whether by early cementation (e.g. Westphal et al., 2000) or via pressure dissolution (Ricken, 1986) and in extreme cases rhythms are lost by amalgamation of beds (Hallam, 1964). Instead, dolomite cementation is pervasive in E3 and appears to develop continuously over a range of shallow depths in all sedimentary beds, being accompanied by local overpressuring and deformation of surface sediments by released fluids.

In summary, given the limited role for diagenetic carbonate redistribution between layers, we infer that the cyclicity is mainly a function of a weak primary variation in sediment texture and/ or carbonate to siliciclastic ratio. The lack of clustering of cycles or strong gradients in any descriptive parameter within the

E3 sediments contrasts with autocyclic systems where internal progradational processes generate cycles whose stacking is a function primarily of accommodation space and which therefore cannot capture aspects of external drivers such as hierarchical stacking of cycles (Pollitt et al. 2015). In contrast, E3 cyclic sediments can be confidently interpreted as displaying allocyclicity, in which a subtle change in composition is imposed on a fine-grained sediment deposited far from sediment sources Ricken (1986), typically by climatic forcing (Elrick and Hinnov, 2007; Weedon, 1993). We return to the timescale of variation in the discussion.

4.3 The E3-E4 transition and the origin of mineral pseudomorphs

The overall succession from E3 to E4 (Fig. 2) has been previously interpreted to be a single regressive unit, culminating in exposure under periglacial conditions corresponding to the base of the Wilsonbreen Formation (Fairchild & Hambrey, 1984). Here, we present new data mainly related to the E3-E4 transition and re-assess the origin of pseudomorphs and crack-fillings across the interval of rapid shoaling.

The northern three sections show a homologous succession from the dolomitic silt-shales of the main part of E3, to increasingly well-sorted siltstones arranged in distinct, thick laminae (Fig. 18A), with the thickest examples being graded and some displaying basal gutter casts or wave-generated cross-laminae. Locally, desiccation cracks or mudclasts (Fig. 18C) occur. These sediments pass up transitionally into dolarenites at the base of E4, locally seen to contain parallel laminated to cross-stratified ooids. This transition is similar to a thick shallowing upwards parasequence from the Ediacaran of Northeast Greenland (Fairchild & Herrington, 1989), where storm-dominated facies pass up into intermittently exposed lagoonal and tidal sandflat facies. Distinctive, but rare sedimentary structure in basal E4 sediments are ptlygmatically folded, crack-fillings, up to 3 cm high and ~ 1 mm wide. They are filled with sediment from relatively coarse sediment layers and cutting finer layers (Fig. 18B). They can be classified as sub-aqueous shrinkage or diastasis cracks (cf. Fairchild & Herrington, 1989; Cowan & James, 1992). This explanation could also apply to the dolomitized structures identified by Hoffman et al. (2012) from a similar horizon in Nordaustlandet to the north of the study area and identified as molar tooth structures which otherwise are not found after initial Cryogenian glaciation locally (Fairchild & Hambrey, 1995) or globally (Kuang, 2014; Shields, 2002, Shields-Zhou et al., 2012).

Pseudomorphs were recorded by Fairchild & Hambrey (1984), both at the top of E3 as numerous small crystal pseudomorphs, typically preserved as moulds, and within E4 as somewhat larger nodular structures, typically replaced by silica. Anhydrite inclusions were noted in the latter case. In the current work, crystal pseudomorphs are found to be restricted to top of E3, within 10 m of the top at Dracöisen, and in a narrower range at Ditlovtoppen. In contrast, Hoffman et al. (2012) showed the pseudomorphs to be distributed in the upper third of E3 in a less well-exposed section in Nordaustlandet to the north of our study area. The pseudomorphs are typically 2-3 mm across and equant, although with a range from obtuse, to right-angled and acute interfacial angles (Fig. 18C), which Halverson et al. (2004) noted were consistent with the cold-water carbonate ikaite ($\text{CaCO}_3 \cdot 6\text{H}_2\text{O}$), although not diagnostic of it. Halverson et al. (2004) showed $\delta^{18}\text{O}$ in the range -15 to -10‰ in examples filled by burial diagenetic calcite spar. At Reinsryggen, pseudomorphs are also preserved locally as calcite spar cement, but also associated with replacive silica (megaquartz), containing inclusions of anhydrite (Fig. 18D). The characteristically larger, nodular pseudomorphs locally found in member E4 consist of a mixture of megaquartz with anhydrite inclusions (Fig. 18F) and vug-lining ferroan saddle dolomite (Fig. 18E). The presence of anhydrite inclusions implies original gypsum (consistent with acute-angled pseudomorphs) or anhydrite (consistent with equant shape and castellated right-angled margins of some pseudomorphs). Calcium sulphate evaporites are indicative of a mildly evaporative depositional environment consonant with a very shallow water setting transitional to the overlying intraclastic and ooidal dolomites with local replaced anhydrite nodules in member E4 (cf. Fairchild & Harrington, 1989). Conversely, the depositional setting is not one where ikaite would be expected (Oehlerich et al., 2013) and contrasts with the varved limestones with ice-rafted debris where ikaite pseudomorphs have been recognized in the overlying Wilsonbreen Formation (Fairchild et al., 2016).

In the southern part of the study area, Halverson et al. (2004) noted the occurrence of a limestone interval at least 5 m thick at the top of E3 at Slangen (5 km west of Backlundtoppen) and here we document a 20 m limestone interval at the north Backlundtoppen section separating dolomitic silt-shales below and oolitic dolomites above (Fig. 2). Sedimentary structures in this interval include guttered bed bases,

hummocky cross-stratification, and two distinct metre-thick stromatolite biostrome horizons. These structures are all consistent with an environment above storm wave-base and transitional upwards to peritidal sediments (e.g. Fairchild & Herrington, 1989; Knoll & Swett, 1990).

Member E4 contains three distinct lithological units (Fairchild & Hambrey, 1984 and Fig. 2). The lowest, unit A, consists of parallel-laminated and cross-stratified ooidal dolarenites (A) interpreted as tidal sandflat deposits, and which is particularly thick at Backlundtoppen overlying the limestone unit. It is overlain by cemented fenestral ooidal dolomites with tepee structures indicative of saline artesian groundwater discharge (B) in a supratidal setting. At Ditlovtoppen, there is an overlying more variable unit with micritic, locally shaly and brecciated dolomites (C), possibly back-barrier in origin. Further north, in Nordaustlandet, E4 is transitional to a sandstone unit (the Bråvika Sandstone), interpreted as fluvial in origin by Hoffman et al. (2012). Deposition of all these units was followed by subaerial exposure and evidence of periglacial conditions: decimetre-scale folds in unit C and extensive development of parallel fracture networks of previously cemented dolomite (Fairchild & Hambrey, 1984). Benn et al. (2015) associate these phenomena with Snowball-type glacial conditions, inferring a multi-million year hiatus.

5. Chronology and Sr isotopes

5.1 Detrital zircon constraints on age

Hopes of constraining depositional age through detrital zircon ages were raised by the presence of rare altered volcanic clasts in E2 (Harland et al., 1993). Also, a volcanic contribution to the E3 shales is indicated by elevated Ti/Al ratios (Kunzmann et al., 2015). Detrital zircons from four sandstones from near the top of member E1 have ages ranging from ca. 2.7 Ma to ca. 1.0 Ga (supplementary Table S4). The age distribution is characterized by a broad dominant major peak from 1.0 Ga to 1.7 Ga and a subordinate population of dates from 2.5 Ga to 2.7 Ga. The spectrum of the E1 samples is comparable to spectra obtained for the Moine Supergroup in Scotland and the main peak at 1.2 Ga is probably linked to the Grenville orogen (Cawood et al. 2007). Detrital zircons in a sample from the Wilsonbreen Formation exhibit comparable age spread to the E1 samples (supplementary Table S5). The youngest statistically significant set of detrital zircon dates from these samples is ca. 1.0 Ga; younger dates are not concordant and likely reflect post-crystallisation Pb-loss.

5.2 Sr isotope chemostratigraphy

Marine carbonates are the most widely used materials for chemostratigraphy and their primary Sr isotope signature has proved less ambiguous than $\delta^{13}\text{C}$ in global correlations (Halverson et al., 2010). In practice, the ratio of radiogenic ^{87}Sr to stable ^{86}Sr tends to increase during diagenesis because of the lowering of Sr content during carbonate stabilization and the addition of ^{87}Sr from Rb-decay in silicates. Common screening criteria are low Rb/Sr, high Sr, and low Mn/Sr (Fairchild et al., 2000; Melezhik et al., 2015), the latter arising from the assumption in Phanerozoic studies that primary Mn would be negligible in concentration, but that it would increase during meteoric diagenesis (Brand & Veizer, 1980). However, significant levels of primary Mn can occur in Neoproterozoic depositional environments (e.g. Hood & Wallace, 2014) and Mn can also be high in fluids during early marine diagenesis as has been established above for E3 dolomitic shales. In our work, only limestones had sufficiently high Sr concentrations to be considered. These were found in both the basal E3 section and the upper E3 section in the Backlundtoppen area (Fig. 19).

For the basal E3 limestones, $^{87}\text{Sr}/^{86}\text{Sr}$ decreases with increasing Sr content (Fig. 19A), but the maximum Sr concentration is only 705 ppm (Supplementary Information, Table S1). Mn/Sr shows less systematic distribution (Fig. 19B) which is unsurprising given the petrographic evidence for growth spikes in Mn (bright CL) during growth in early marine diagenesis. Nevertheless the sample with highest Sr and lowest Mn/Sr yields the lowest Sr isotope ratio of 0.70717. The primary seawater signature can be safely inferred to be <0.7072 , but could be rather lower given the relatively low Sr content of the sample suite.

The limestones near the top of E3 are more conventional (allochemical and stromatolitic) and form the base of a regressive package implying that they may have been subjected to meteoric diagenesis. Here, a wider range of Sr concentrations was encountered, and the $^{87}\text{Sr}/^{86}\text{Sr}$ values approach an asymptote with higher Sr concentrations, with a low of 0.70767 found in a sample with 1079 ppm Sr. This least altered sample, with over 1000 ppm Sr and $\text{Mn}/\text{Sr} < 0.1$ would pass the rigorous screening criteria used in previous literature (Fairchild et al., 2000) and a primary Sr isotope signature of close to 0.70765 is implied.

These new data from Svalbard show a similar overall trend to values in the LCWI elsewhere, but are slightly more radiogenic. Typical early post-Sturtian strontium isotope compositions are $\sim 0.7067\text{--}0.7069$, rapidly rising to a plateau of $0.7071\text{--}0.7073$, with a single (pre-Trezona anomaly) value as high as 0.70735 (Kaufman et al., 1997; Shields et al., 1997; McKirdy et al., 2001; Halverson et al., 2007). Early Ediacaran $^{87}\text{Sr}/^{86}\text{Sr}$ values are nearly identical to typical pre-Marinoan values: ~ 0.7072 (James et al., 2001; Halverson et al., 2007), but these rise sharply to ratios in excess of 0.7077 within the basal Ediacaran cap carbonate sequence (Halverson et al., 2010). Hence, whereas the lower E3 values resemble basal Ediacaran values, upper E3 values are too unradiogenic to reflect middle Ediacaran values. Therefore, either the screening criteria are invalid for the basal E3 limestones, or the elevated values reflect deposition at a time when local seawater was heavily influenced by glacial meltwater. The latter hypothesis is consistent with the oxygen isotope evidence presented above. The elevated upper E3 values are more ambiguous. Either they capture a highly radiogenic pre-Marinoan seawater composition otherwise not seen in other successions, or they reflect restriction of the basin and Sr reservoir influenced by local runoff. We favour the latter hypothesis based on the mineralogical evidence for increasing restriction of the basin discussed above and the coherent carbon isotope profile through E3–E4 that implies that these rocks entirely pre-date the Trezona $\delta^{13}\text{C}$ anomaly.

6. Discussion

6.1 Palaeoenvironmental evolution

The Cryogenian period is thought to have had low concentrations of atmospheric oxygen and highly variable PCO_2 (Fairchild & Kennedy, 2007; Bao et al., 2009). Available evidence suggests anoxic oceans (largely ferruginous but locally euxinic) beneath an oxygenated surface mixed layer (Och & Shields-Zhou, 2012; Tahata et al., 2015; Sperling et al., 2015). This model, based on redox proxies, is consistent with petrographic evidence from the LCWI in South Australia, where primary dolomite cements in a reef complex with significant vertical relief record gradients in Fe and Mn (Hood & Wallace, 2014, 2015). Our geochemical and petrographic data from the middle of E3, which show significant Fe and Mn enrichment, are consistent with anoxic bottom waters.

The base of Member E3 is transitional with marine glacial deposits and continues into the shaly carbonates that characterize most of the member and display the characteristic mid-Cryogenian negative to positive $\delta^{13}\text{C}$ profile. These features imply that that deposition at the base of E3 begins during the transition to a highstand, consistent with Sturtian cap carbonates globally (Kennedy et al., 1998; Hoffman & Schrag, 2002). This pattern contrasts sharply with the falling $\delta^{13}\text{C}$ profile recorded in a transgressive systems tract at the base of Marinoan cap carbonates (Kennedy et al., 1998; Hoffman and Schrag, 2002; Halverson et al., 2004).

The duration of cap carbonate deposition and the meaning of the $\delta^{13}\text{C}$ anomaly has been actively debated (Trindade et al., 2003; Hoffman et al., 2007; Kennedy & Christie-Blick, 2011), but limitations on the hydrological cycle revealed through modelling indicate that high PCO_2 conditions would have persisted for up to millions of years post-glacially (Le Hir et al., 2009). It is currently unclear whether the changing $\delta^{13}\text{C}$ value reflects bathymetry or changing ocean chemistry (Kaufman et al., 1997; Giddings & Wallace, 2009a). Nevertheless, a distinct stratification forced by meltwater influx is distinctly possible as is active carbonate production stimulated by photosynthetic blooms (Shields, 2005). In the base of E3, like Sturtian caps in general, there is evidence for the rapid stabilization of metastable carbonate to either dolomite or calcite, possibly microbially mediated.

Cyclic shale facies like those in Svalbard occur in the immediately post-Sturtian Tapley Hill Formation, (Giddings et al., 2009), but there, as in Namibia, purer carbonate deposition subsequently dominates the platform stratigraphy. Svalbard is unusual then, in that consistent depositional environment and lithology is maintained through most of the LCWI. A consistent shale environment is also found in the Datangop Formation of South China (Li et al., 2012), but cyclicity is not documented. The carbon isotope pattern in E3 is similar to other sections of the LCWI, but roughly 2‰ lower. Given the potential for bathymetric variation in $\delta^{13}\text{C}$ (Giddings & Wallace, 2009b) and a component of authigenic carbonate, this difference in $\delta^{13}\text{C}$ is not significant.

The upper part of the succession is a well-developed regressive sequence 25-40 m in thickness, culminating in subaerial exposure. Conditions were mildly evaporitic in most of the basin, leading to the preservation of pseudomorphs of calcium sulphates, including some previously interpreted as ikaite. More typical shallow subtidal, storm-influenced limestones characterize the base of the shallowing upwards interval in the south of the study area indicative of a more open marine connection. The South Australian and NW Canadian sections between glacials include a well-developed progradational upper unit containing variably high $\delta^{13}\text{C}$ values and a distinct negative (Trezona) anomaly that is also found in several other regions (Halverson and Shields-Zhou, 2011). The absence of this feature suggests top-truncation of the pre-Marinoan succession in Svalbard. This truncation could have been relatively minor if the regression itself reflected the initial build-up of Marinoan ice at high latitudes, but there are no chronostratigraphic constraints to confirm such a timing, and Halverson et al. (2002) argued that the onset of the Trezona anomaly pre-dated glacieustatic sea level fall related to onset of Marinoan glaciation.

The uppermost surface of E4 at the base of the Wilsonbreen Formation has been interpreted (Benn et al., 2015) as a multi-million year hiatus, coinciding with a deep-frozen Snowball Earth condition culminating in periglaciation and glacialfluvial erosion, followed by ice advances and retreats in a terrestrial setting. This represents a late stage in the glaciation when PCO_2 had risen to high levels (Bao et al., 2009; Benn et al., 2015).

6.2 Astronomical forcing and the time interval duration of the LCWI

The striking rhythmicity of E3 is interpreted above as allocyclic. Given the radiometric constraints that the total duration of the LCWI is 5-27 Myr, but that the succession in Svalbard is top-truncated, it is likely to represent 3-20 Myr of deposition. Given also that there are nearly 300 cycles observed at Ditlovtoppen, a first pass at estimating cycle duration is that they should represent between 10 kyr and 66 kyr, within the Milankovitch band.

Cycles corresponding to each of the main Milankovitch bands between 20 and 400 kyr are well-preserved in appropriate settings in the geological record (Hinnov, 2013; Hilgen et al., 2015). Study of such cyclicity in pelagic sediments has provided a calibration of $^{40}\text{Ar}/^{39}\text{Ar}$ geochronology and the definitive age of the Mesozoic-Cenozoic boundary (Kuiper et al., 2008). Older successions are subject to more uncertainty, but there exist a large number of successful studies in the Mesozoic and increasingly in the Palaeozoic (Hinnov, 2013) and even the Mesoproterozoic (Zhang et al., 2015) where multiple frequencies have been identified and assigned to particular bands. One source of change is the effect of increasing Earth-Moon distance over time, which is incompletely known. However, Waltham (2015) has calculated both the changing periodicity and estimated the associated uncertainties.

In both early and late-Cryogenian times, NE Svalbard is thought to have lain in the tropics or sub-tropics (Li et al., 2013), latitudes which are particularly susceptible to the effects of precessional forcing (e.g. Wang et al., 2008), in contrast to obliquity forcing at high latitudes. Hence precessional forcing is our preferred hypothesis for the E3 cycles. In the overlying Wilsonbreen Formation, Benn et al. (2015) have shown through climate modelling that glacial advances and retreats in the latter stages of a Snowball Earth ice age are consistent with aridity-humidity shifts on precessional timescales. At 650 Ma, the four precessional frequencies, which today are 18.95, 19.1, 22.4 and 23.7 kyr, then were 16.3, 16.4, 18.8 and 19.7 kyr with uncertainties between 1.4 and 1.9 kyr (Waltham, 2015). A generalized figure of 18 kyr will be used here.

Two examples of strong stratigraphic signals of precession in Palaeozoic sediment illustrate the extremes of sedimentation rates in which precessional signals are likely to be preserved. The classic Aptian cored section at Piobbico, Italy (Huang et al., 2010) which displays prominent precessional cycles in

greyscale variation is composed of pelagic carbonate sediments that accumulated exceptionally slowly at around 0.5 cm/kyr (post-compaction and corresponding to around 10 cm per cycle). This contrasts with the Triassic rift-related Newark Group where shallowing upwards precessional cycles around 5 m thick in lacustrine lithofacies were controlled by humidity-aridity variations (Olsen & Kent, 1996). The 0.5 m modal thickness of E3 cycles is comfortably within this variation and implies a deep-shelf mudrock accumulation rate of around 2.8 cm/kyr, which is within the range of pelagic sediments. The inferred accumulation rate is slightly lower than that of various deep-water Palaeozoic cyclic carbonates with limestone-marl couplets 4-20 cm thick that are interpreted as millennial cycles (Elrick and Hinnov, 2007).

Now we attempt a more careful estimate of time duration recorded by the E3-E4 succession. The uppermost part of E3 and member E4 represent a regressive sequence which could have accumulated relatively quickly and so are disregarded, leaving 200 m thickness of E3. The maximum number of *observed* cycles was 270, between 12 m and 195 m stratigraphic height at Ditlovtoppen, which would scale to 300 over 200 m thickness, providing an estimate of the minimum number of cycles. An upper bound of 400 cycles is set if one takes the true modal thickness of cycles to be 0.5 m on average, i.e. assuming that larger apparent thicknesses are due to missed cycles. Hence, the duration of E3 can be estimated to be of 5.4 to 7.2 Myr (based on 300 to 400 cycles of 18 ka duration) which is close to the minimum estimate from geochronology deduced in the introduction. However in South Australia, Namibia and NW Canada, the Trezona carbon isotope anomaly takes up the upper 5-10% of the LCWI (Halverson et al., 2005) and this is missing in Svalbard, implying that the duration should be estimated in round figures at 6 to 8 Myr, assuming that accommodation space had limited deposition only in the immediately pre-Marinoan period.

7. Conclusions

1. The presumed correlation of members E3 and E4 with the LCWI is supported by the discovery of a well-developed $\delta^{13}\text{C}$ profile and lithologies typical of Sturtian cap carbonates overlying marine glacial deposits of member E2. Primary Sr isotope values determined from limestones in the south of the study area of <0.7072 at the base of E3, and 0.7076 at the top are consistent with this.
2. The possible ikaite pseudomorphs previously described from the top of E3, are shown to have originally been calcium sulphate, consistent with the evaporative environment of overlying E4.
3. The sub-E2 $\delta^{13}\text{C}$ anomaly, correlated with the pre-Marinoan Trezona anomaly in Halverson et al. (2004), is now understood to be the pre-Sturtian Islay anomaly, consistent with Sr-isotope evidence. The lack of preservation of a Trezona anomaly implies that the section between the glaciations is top-truncated, consistent with the supratidal sediments at the top of E4.
4. The smooth $\delta^{13}\text{C}$ profile in E3, despite the Fe- and Mn-rich nature of the carbonates, points to an unexpectedly limited role for organically mediated diagenesis in these shaly sediments. There is a contrast between carbonates at the base of E3 and in the main part of this member. At the base of E3, all crystals of dolomite or calcite as one horizon show the same CL zonation replacing a less stable precursor phase, probably precipitated in the water column, and which could be ikaite. In the main part of E3, Fe- and Mn-rich dolomites show much more variable CL properties indicating diachronous growth, although still during early diagenesis as demonstrated by local non-compacted concretions. Consistent $\delta^{13}\text{C}$ implies buffering by pre-existing carbonate phase and fits with the low organic content of the sediments. Fe- and Mn-reduction likely occurred in the surficial zone or in the water column, although the presence of some ^{13}C -depleted, Fe- and Mn-rich, pore-filling calcite indicates continued Fe- and Mn-supply deeper in the sediment.
5. Centimetre-scale disturbance structures in mid-E3 are reconstructed to be horizontal prolapses (sheath-like folds) of microbially bound and unlithified surficial sediments. They may be characteristic of fluid escape from underlying sediments undergoing active cementation.
6. Subtle variations in carbonate and siliciclastic content give rise to the allocyclic sedimentary rhythms that are the dominant feature of well-weathered outcrops of E3. Where most completely exposed, modal cycle thickness is 0.5 m. If the cycles are forced by precession, as is consistent with the low palaeolatitude, the preserved thickness of the interval between glaciations represents a time period of 6-8 Myr.

Acknowledgements

This work was supported by the NERC-funded project GR3/NE/H004963/1 Glacial Activity in Neoproterozoic Svalbard (GAINS). Logistical underpinning of our helicopter-supported fieldwork was provided by the University Centre in Svalbard and the Svalbard Governor's Office, facilitated by our collaborator Doug Benn. We acknowledge the following for their essential help: Dan Condon (zircon work at NIGL), Imran Rahman (SPIERS software), David Limmer and Paula Boomer (sample preparation), Ian Boomer (stable isotope analysis), Nick Marsh (XRF analysis), Paul Stanley (SEM) and John Craven (ion microprobe). Paul Hoffman and Nick Christie-Blick are thanked for their referees' comments.

References

- Arnaud, E. & Fairchild, I.J. 2011 The Port Askaig Formation, Dalradian Supergroup, Scotland In: Arnaud, E., Halverson, G. P. & Shields-Zhou, G. (eds) *The Geological Record of Neoproterozoic glaciations*. Geological Society of London, Memoir, 36, 635-642.
- Bao, H., Fairchild, I.J., Wynn, P.M., Spötl, C., 2009. Stretching the envelope of past surface environments: Neoproterozoic glacial lakes from Svalbard. *Science*, 323, 119-122.
- Benn, D.I., Le Hir, G., Bao, H., Donnadieu, Y., Dumas, C., Fleming, E.J., Hambrey, M.J., McMillan, E.A., Petronis, M.S., Ramstein, G., Stevenson, C.T.E., Wynn, P.M., Fairchild, I.J., 2015. Orbitally forced Ice sheet fluctuations at the end of the Marinoan Snowball Earth glaciation. *Nature Geoscience*, DOI: 10.1038/NNGEO2502.
- Beraldi-Campesi, H., Farcia-Pichel, F., 2011. The biogenicity of modern terrestrial roll-up structures and significance for ancient life on land. *Geobiology*, 9, 10-23.
- Bosak, T., Newman, D.K. 2003. Microbial nucleation of calcium carbonate in the Precambrian. *Geology*, 31, 577-580.
- Bowring, S.A., Grotzinger, J.P., Condon, D.J., Ramezani, J., Newall, M.J., Allen, P.A., 2007. Geochronologic constraints on the chronostratigraphic framework of the Neoproterozoic Huqf Supergroup Sultanate of Oman. *American Journal of Science*, 307, 1097-1145.
- Brand, U., Veizer, J., 1980. Chemical diagenesis of a multicomponent carbonate system. 1. Trace elements. *Journal of Sedimentary Petrology*, 50, 1219-1236.
- Calver, C.R., Crowley, J.L., Wingate, M.T.D., Evans, D.A.D., Raub, T.D., Schmitz, M.D., 2013. Globally synchronous Marinoan deglaciation indicated by U-Pb geochronology of the Cottons Breccia, Tasmania, Australia. *Geology*, 10, 1127-1130.
- Cawood, P.A., Nemchin, A.A., Strachan, R., Prave, T., Krabbendam, M., 2007. Sedimentary basin and detrital zircon record along East Laurentia and Baltica during assembly and breakup of Rodinia. *Journal of the Geological Society, London*, 164, 257-275.
- Charlier, B.L., Ginibre, C., Morgan, D., Nowell, D., Pearson, D.G., Davidson, J.P., Ottley, C.J. 2006. Methods for the microsampling and high-precision analysis of strontium and rubidium isotopes at single crystal for petrological and geochronological applications. *Chemical Geology*, 232, 114-133.
- Chew, S.C., Kundukad, B., Seviour, T., van der Maarel, J.R.C., Yang, L., Rice, S.A., Doyle, P., Kjelleberg, S., 2014. Dynamic remodelling of microbial biofilms by functionally distinct exopolysaccharides. *mBio*, 5(4):e01536-14. doi:10.1128/mBio.01536-14.
- Condon, D., Zhu, M., Bowring, S., Wang, W., Yang, A., Jin, Y. 2005. U-Pb ages from the Neoproterozoic Doushantuo Formation, China. *Science*, 308, 95-98.
- Cowan, C.A. and James, N.P., 1992. Diastasis cracks: mechanically generated synaeresis-like cracks in Upper Cambrian shallow water oolite and ribbon carbonates. *Sedimentology*, 39, 1101-1118.
- Day, E.S., James, N.P., Narbonne, G.M., Dalrymple, R.W., 2004. A sedimentary prelude to Marinoan glaciation, Cryogenian (Middle Neoproterozoic) Keele Formation, Mackenzie Mountains, northwestern Canada. *Precambrian Research*, 133, 223-247.
- Elrick, M., Hinnov, L.A., 2007. Millennial-scale palaeoclimate cycles recorded in widespread deeper water rhythmites of North America. *Palaeogeography, Palaeoclimatology, Palaeoecology*, 243, 348-372.

- Fairchild, I.J., 1991. Origins of carbonate in Neoproterozoic stromatolites and the identification of modern analogues. *Precambrian Research*, 53, 281-299.
- Fairchild, I.J., Hambrey, M.J., 1984. The Vendian succession of northeastern Spitsbergen – petrogenesis of a dolomite-tillite association. *Precambrian Research*, 26, 111-167.
- Fairchild, I.J., Hambrey, M.J., 1995. Vendian basin evolution in East Greenland and NE Svalbard. *Precambrian Research*, 73, 217-233.
- Fairchild, I.J., Herrington, P.M., 1989 A tempestite-evaporite-stromatolite association (late Vendian, East Greenland): a shoreface-lagoon model. *Precambrian Research*, 43, 101-127
- Fairchild, I.J., Spiro, B. 1987. Petrological and isotopic implications of some contrasting Precambrian carbonates, NE Spitsbergen. *Sedimentology*, 34, 973-989.
- Fairchild, I.J., Kennedy, M.J., 2007. Neoproterozoic glaciation in the Earth System. *Journal of the Geological Society, London*, 164, 895-921.
- Fairchild, I.J., Spiro, B., Herrington, P.M., Song, T. 2000. Controls on Sr and C isotope compositions of Neoproterozoic Sr-rich limestones of E Greenland and N China, In: Grotzinger, J.P., James, N.P. (eds.) *Carbonate Sedimentation and Diagenesis in the Evolving Precambrian World* SEPM Special Publication 67, 297-313.
- Fairchild, I.J., Fleming, E.J., Bao, H., Benn, D.I., Boomer, I., Dublyansky, Y.V., Halverson, G.P., Hambrey, M.J., Hendy, C., McMillan, E.A., Spötl, C., Stevenson, C.T.E., Wynn, P.M., 2016 Continental carbonate facies of a Neoproterozoic panglaciation, NE Svalbard. In revision for *Sedimentology*.
- Fleming, E.J., 2014. Magnetic, structural and sedimentological analysis of glacial sediments: insights from modern, Quaternary and Neoproterozoic environments. University of Birmingham, unpubl. PhD. thesis, <http://etheses.bham.ac.uk/5136/>
- Giddings, J.A., Wallace, M.W., 2009a. Sedimentology and C-isotope geochemistry of the 'Sturtian' cap carbonate, South Australia. *Sedimentary Geology*, 216, 1-14.
- Giddings, J.A., Wallace, M.W., 2009b. Facies dependent $\delta^{13}\text{C}$ variation from a Cryogenian platform margin, South Australia: Evidence for stratified Neoproterozoic oceans? *Palaeogeography, Palaeoclimatology, Palaeoecology*, 271, 196-214.
- Giddings, J.A., Wallace, M.W., Woon, E.M.S., 2009. Interglacial carbonates of the Cryogenian Umberatana Group, northern Flinders Ranges, South Australia. *Australian Journal of Earth Sciences* 56, 907–925.
- Gorjan, P., Veevers, J.J., Walter, M.R., 2000. Neoproterozoic sulfur-isotope variation in Australia and global implications. *Precambrian Research*, 100, 151–179.
- Grey, K., Yochelson, E.L., Fedonkin, M.A., Martin, D. McB., 2010. *Horodyskia williamsii* new species, a Mesoproterozoic macrofossil from western Australia. *Precambrian Research*, 180, 1-17.
- Hallam, A., 1964. Origin of the limestone-shale rhythms in the Blue Lias of England: A composite theory. *Journal of Geology*, 72, 157-168.
- Halverson, G.P., 2006. A Neoproterozoic Chronology In: Xiao, S., Kaufman, A.J. (Eds.) *Neoproterozoic Geobiology and Paleobiology*, Springer, New York, 231-271.
- Halverson, G.P., 2011. Glacial sediments and associated strata of the Polarisbreen Group, northeastern Svalbard. In: Arnaud, E., Halverson, G.P. & Shields-Zhou, G. (eds), *The Geological Record of Neoproterozoic Glaciations*. Geological Society, London, Memoirs, 36, 571-579.
- Halverson, G.P., Shields-Zhou, G., 2011. Chemostratigraphy and the Neoproterozoic glaciations. In: Arnaud, E., Halverson, G.P. & Shields-Zhou, G. (eds), *The Geological Record of Neoproterozoic Glaciations*. Geological Society, London, Memoirs, 36, 51-66.
- Halverson, G.P., Hoffman, P.F., Schrag, D.P., Kaufman, A.J., 2002. A major perturbation of the carbon cycle before the Ghuab glaciation (Neoproterozoic) in Namibia: Prelude to snowball Earth? *Geochemistry, Geophysics, Geosystems*, 3, 1035. doi: 10.1029/2001GC000244.
- Halverson, G.P., Maloof, A.C., Hoffman, P.F., 2004. The Marinoan glaciation (Neoproterozoic) in northeast Svalbard. *Basin Research*, 16, 297-324.
- Halverson, G.P., Hoffman, P.F., Schrag, D.P., Maloof, A.C., Rice, A.H.N., 2005. Towards a Neoproterozoic composite carbon-isotope record. *Geological Society of America Bulletin*, 117, 1181-1207.
- Halverson, G.P., Dudas, F.O., Maloof, A.C., Bowring, S.A., 2007. Evolution of the $^{87}\text{Sr}/^{86}\text{Sr}$ composition of Neoproterozoic seawater. *Palaeogeography, Palaeoclimatology, Palaeoecology* 256, 103-129.

- Halverson, G.P., Wade, B.P., Hurtgen, M.T., Barovich, K.M., 2010. Neoproterozoic chemostratigraphy. *Precambrian Research*, 182, 337-350.
- Hambrey, M.J., 1982. Late Precambrian diamictites of northeastern Svalbard. *Geological Magazine*, 119, 527-551.
- Harland, W.B., Hambrey, M.J., Waddams, P., 1993. Vendian geology of Svalbard. *Norsk Polaristitut Skrifter*, 193.
- Hilgen, F.J., Hinnov, L.A., Aziz, H.A., Abels, H.A., Batenbrug, S., Bosmans, J.H.C., de Boer, B., Hüsing, S.K., Kuiper, K.F., Lourens, L.J., Rivera, T., Ruenter, E., van de Wal, R.S.W., Wotzlaw, J.-F., Zeeden, C. 2015 Stratigraphic continuity and fragmentary sedimentation: the success of cyclostratigraphy as part of integrated stratigraphy. In: Smith, D. G., Bailey, R. J., Burgess, P.M., Fraser, A. J. (eds) *Strata and Time: Probing the Gaps in Our Understanding*. Geological Society, London, Special Publications, 404, 157-197.
- Hinnov, L.A., 2013. Cyclostratigraphy and its revolutionizing applications in the earth and planetary sciences. *Geological Society of America Bulletin*, 125, 1703-1734.
- Hoffman, P.F., 2011. Strange bedfellows: glacial diamictite and cap carbonate from the Marinoan (635 Ma) glaciations in Namibia. *Sedimentology*, 58, 57-119.
- Hoffman, P.F., Schrag, D.P., 2002. The snowball Earth hypothesis: testing the limits of global change. *Terra Nova*, 14, 129-155.
- Hoffman, P.F., Halverson, G.P. 2008. Otavi Group of the western Northern Platform, the Eastern Kaoko Zone and the western Northern Margin Zone. In: Miller, R. McG. (ed.) *The Geology of Namibia*, vol. 2. Geological Survey of Namibia, Windhoek, Namibia, 13-69 – 13-136.
- Hoffman, P.F., Halverson, G.P., Domack, E.W., Husson, J.M., Higgins, J.A. and Schrag, D.P., 2007. Are basal Ediacarn (635 Ma) post-glacial “cap dolostones” diachronous? *Earth and Planetary Science Letters*, 258, 114-131.
- Hoffman, P.F., Halverson, G.P., Domack, E.W., Maloof, A.C., Swanson-Hysell, N.L., Cox, G.M., 2012. Cryogenian glaciations on the southern tropical paleomargin of Laurentia (NE Svalbard and East Greenland), and a primary origin for the upper Russøya (Islay) carbon isotope excursion. *Precambrian Res.*, 206-207, 137-158.
- Hoffmann, K.-H., Condon, D.J., Bowring, S.A., Crowley, J.L. 2004. U-Pb zircon date from the Neoproterozoic Ghaub Formation, Namibia: Constraints on Marinoan glaciation. *Geology*, 32, 817-820.
- Hofmann, H.J., Narbonne, G.M., Aitken, J.D. 1990. Ediacarian remains from intertillite beds in northwestern Canada. *Geology*, 18, 1199–1203.
- Hood, A.V.S., Wallace, M.W., 2014 Marine cements reveal the structure of an anoxic, ferruginous Neoproterozoic ocean. *Journal of the Geological Society, London*, 171, 741-744.
- Hood, A.V.S, Wallace, M.W., 2015. Extreme ocean anoxia during the Late Cryogenian recorded in reefal carbonates of Southern Australia. *Precambrian Research*, 261, 96-111.
- Huang, C., Hinnov, L., Fischer, A.G., Grippo, A., Herbert, T., 2010. Astronomical tuning of the Aptian Stage from Italian reference sections. *Geology*, 38, 899-902.
- Hurtgen, M.T., Arthur, M.A., Suits, N., Kaufman, A.J., 2002. The sulfur isotopic composition of Neoproterozoic seawater sulfate: implications for snowball Earth? *Earth and Planetary Science Letters* 203, 413–429.
- IUGS (International Union of Geological Sciences) 2014 International Commission on Stratigraphy, Annual Report 2014. <http://iugs.org/uploads/ICS%202014.pdf>. Accessed 16th March 2015.
- Irwin, H., Curtis, C., Coleman, M., 1977. Isotopic evidence for source of diagenetic carbonates formed during burial of organic-rich sediments. *Nature*, 269, 209-213.
- James, N.P., Narbonne, G.M., Kyser, T.K., 2001. Late Neoproterozoic cap carbonates: Mackenzie Mountains, northwestern Canada: precipitation and global glacial meltdown. *Canadian Journal of Earth Sciences*, 38, 1229-1262.
- Kaufman, A.J., Knoll, A.H., Narbonne, G.M. 1997. Isotopes, ice ages, and terminal Proterozoic earth history. *Proceedings of the National Academy of Sciences, USA*, 94, 6600-6605.
- Kendall, B., Creaser, R.A., Selby, D. 2006. Re-Os geochronology of post-glacial black shales in Australia: Constraints on timing of “Sturtian” glaciation. *Geology*, 34, 729-732.
- Kendall, B., Creaser, R.A., Calver, C.R., Ruab, T.D., Evans, D.A.D., 2009. Correlation of Sturtian diamictite successions in southern Australia and northwestern Australia by Re-Os black shale geochronology and

- the ambiguity of “Sturtian”-type diamictite-cap carbonate pairs as chronostratigraphic marker horizons. *Precambrian Research*, 172, 301-310.
- Kennedy, M.J., Christie-Blick, N., 2011. Condensation origin for Neoproterozoic cap carbonates during deglaciation. *Geology*, 39, 319-322.
- Kennedy, M.J., Runnegar, B., Prave, A.R., Hoffman, K.-H., Arthur, M.A. 1998. Two or four Neoproterozoic glaciations? *Geology*, 26, 1059-1063.
- Knoll, A.H., Swett, K., 1990. Carbonate deposition during the Late Proterozoic Era: an example from Spitsbergen. *American Journal of Science*, 290-A, 104-132.
- Knoll, A.H., Hayes, J.M., Kaufman, A.J., Swett, K., Lambert, I.B. 1986. Secular variation in carbon isotope ratios from Upper Proterozoic successions of Svalbard and East Greenland. *Nature*, 321, 832-838.
- Kuang, H.-W., 2014 Review of molar tooth structure research. *Journal of Palaeogeography*, 3, 359-383.
- Kuiper, K.F., Deino, A., Hilgen, F.J., Krigsman, W., Renne, P.R., Wijbrans, J.R., 2008. Synchronizing rock clocks of Earth history. *Science*, 320, 500-504.
- Kunzmann, M., Halverson, G.P., Scott, C., Minarik, W.G., Wing, B.A., 2015. Geochemistry of Neoproterozoic black shales from Svalbard: Implications for oceanic redox conditions spanning Cryogenian glaciations. *Chemical Geology*, 417, 383-393.
- Lan, Z., Li, X., Zhu, M., Chen, Z.-Q., Zhang, Q., Li, Q., Lu, D., Liu, Y., Tang, G., 2014. A rapid and synchronous initiation of the widespread Cryogenian glaciations. *Precambrian Research*, 255, 401-411.
- Land, L.S., 1980. The isotopic and trace element geochemistry of dolomite: the state of the art. In Zenger, D.H., Dunham, J.B. & Ethington, R.L. (eds.), *Concepts and Models of Dolomitization*, SEPM Special Publication, 28, 87-110.
- Lawrence, M.J.F., Hendy, C.H., 1985. Water column and sediment characteristics of Lake Fryxell, Taylor Valley, Antarctica. *New Zealand Journal of Geology and Geophysics*, 28, 543-552.
- Le Heron, D.P., Cox, G.M., Trundle, A.E., Collins, A., 2011. Sea-ice free conditions during the early Cryogenian (Sturt) glaciation, South Australia. *Geology*, 39, 31-34.
- Le Heron, D.P., Busfield, M., Kamona, F., 2013. An interglacial on Snowball Earth? Dynamic ice behaviour revealed in the Chuos Formation, Namibia. *Sedimentology*, 60, 411-427.
- Le Hir, G., Donnadiou, Y., Godd  ris, Y., Pierrehumbert, R.T., Halverson, G.P., Macouin, M., N  d  lec, A., Ramstein, G., 2009. The Snowball Earth aftermath: Exploring the limits of continental weathering processes. *Earth and Planetary Science Letters*, 277, 453-463.
- Leather, J., Allen, P.A., Brasier, M.D., Cozzi, A. 2002. Neoproterozoic snowball Earth under scrutiny: Evidence from the Fiq glaciation of Oman. *Geology*, 30, 891-894.
- Li, C., Love, G.D., Lyons, T.W., Scott, C.T., Feng, L., Huang, J., Chang, H., Zhang, Q., Chu, X., 2012. Evidence for a redox stratified Cryogenian marine basin, Datangpo Formation, South China. *Earth and Planetary Science Letters*, 331-332, 246-256.
- Li, Z.-X., Evans, D.A.D., Halverson, G.P., 2013. Neoproterozoic glaciations in a revised global palaeogeography from the breakup of Rodinia to the assembly of Gondwanaland. *Sedimentary Geology*, 294, 219-232.
- Macdonald, F.A., Jones, D.S., Schrag, D.P., 2009. Stratigraphic and tectonic implications of a newly discovered glacial diamictite-cap carbonate couplet in southwestern Mongolia. *Geology*, 37, 123-126.
- Macdonald, F.A., Schmitz, M.D., Crowley, J.L., Roots, C.F., Jones, D.S., Maloof, A.C., Strauss, J.V., Cohen, P.A., Johnston, D.T., Schrag, D.P., 2010. Calibrating the Cryogenian. *Science* 327, 1241-1243.
- Mazzullo, S.J., 2000. Organogenic dolomitization in peritidal to deep-sea sediments. *Journal of Sedimentary Research*, 70A, 10-23.
- McKirdy, D.M., Burgess, J.M., Lemon, N.M., Yu, X., Cooper, A.M., Gostin, V.A., Jenkins, R.J.F., Both, R.A. 2001. A chemostratigraphic overview of the late Cryogenian interglacial sequence in the Adelaide Fold-Thrust Belt, South Australia. *Precambrian Research*, 106, 149-186.
- Melezhik, V.A., Ihlen, P.M., Kuznetsov, A.B., Gjelle, S., Solli, A., Gorokhov, I.M., Fallick, A.E., Sandstad, J.S., Bjerkg  rd, T., 2015. Pre-Sturtian (800-730 Ma) depositional age of carbonates in sedimentary sequences hosting stratiform iron ores in the Uppermost Allochthon of the Norwegian Caledonides: A chemostratigraphic approach. *Precambrian Research*, 261, 272-299.
- Mortimer, R.J.G., Coleman, M.L., 1997. Microbial influence on the oxygen isotopic composition of diagenetic siderite. *Geochimica Cosmochimica Acta*, 61, 1705-1711.

- Mozley, P.S., Burns, S.J., 1993. Oxygen and carbon isotopic composition of marine carbonate concretions: An overview. *Journal of Sedimentary Petrology*, 63, 73-83.
- Narbonne, G.M., Aitken, J.D., 1995. Neoproterozoic of the Mackenzie Mountains, northwestern Canada. *Precambrian Research*, 73, 101-121.
- Och, L.M., Shields-Zhou, G.A., 2012. The Neoproterozoic oxygenation event: Environmental perturbations and biogeochemical cycling. *Earth-Science Reviews*, 110, 26-57.
- Oehlerich, M., Mayr, C., Griesshaber, E., Lücke, A., Oeckler, O.M., Ohlendorf, C., Schmahl, W.W., Zolitschka, B., 2013. Ikaite precipitation in a lacustrine environment – implications for palaeoclimatic studies using carbonates from Laguna Potrok Alke (Patagonia, Argentina). *Quaternary Science Reviews*, 71, 46-53.
- Olsen, P.E., Kent, D.V., 1996. Milankovitch climate forcing in the tropics of Pangaea during the late Triassic. *Palaeogeography, Palaeoclimatology, Palaeoecology*, 122, 1-26.
- Pollitt, D.A., Burgess, P.M., Wright, V.P., 2015. Investigating the occurrence of hierarchies of cyclicity in platform carbonates. In: Smith, D. G., Bailey, R. J., Burgess, P.M., Fraser, A. J. (eds) *Strata and Time: Probing the Gaps in Our Understanding*. Geological Society, London, Special Publications, 404, 123-150.
- Porada, H., Bouougri, El H., 2007. Wrinkle structures – a critical review. *Earth-Science Reviews*, 81, 199-215.
- Pruss, S.B., Bosak, T., Macdonald, F.A., McLane, M., Hoffman, P.F., 2010. Microbial facies in a Sturtian cap carbonate, the Rasthof Formation, Otavi Group, northern Namibia. *Precambrian Research*, 181, 187-198.
- Ricken, W., 1986. Diagenetic Bedding. A model for Marl-Limestone Alternations. *Lecture Notes in Earth Sciences*, 6. Springer-Verlag, Berlin.
- Ricken, W., 1996. Bedding rhythms and cyclic sequences as documented in organic carbon-carbonate patterns, Upper Cretaceous, Western Interior, U.S. *Sedimentary Geology*, 102, 131-154.
- Riedman, L.A., Porter, S.M., Halverson, G.P., Hurtgen, M.T., Junium, C.K., 2014. Organic-walled microfossil assemblages from glacial and interglacial Neoproterozoic units of Australia and Svalbard. *Geology*, 42, 1011-1014.
- Rieu, R., Allen, P.A., Cozzi, A., Kosler, J., Bussy, F., 2007a. A composite stratigraphy for the Neoproterozoic Huqf Supergroup of Oman: integrating new litho-, chemo- and chronostratigraphy data of the Mirbat area, southern Oman. *Journal of the Geological Society, London*, 164, 997-1009.
- Rieu, R., Allen, P.A., Plotze, M., Pettke, T., 2007b. Compositional and mineralogical variations in a Neoproterozoic glacially influenced succession, Mirbat area, south Oman: Implications for paleoweathering conditions. *Precambrian Research*, 154, 248-265.
- Rimstidt, J.D., Balog, A., Webb, J., 1998. Distribution of trace elements between carbonate minerals and aqueous solutions. *Geochimica et Cosmochimica Acta*, 62, 1851-1863.
- Roberts, N.M., Parrish, R.R., Horstwood, M.S., Brewer, T.S., 2011. The 1.23 Ga Fjellhovdane rhyolite, Grøssæ-Totak; a new age within the Telemark supracrustals, southern Norway. *Norwegian Journal of Geology*, 91, 239-246.
- Rooney, A.D., Macdonald, F.A., Strauss, J.V., Dudás, F.O., Hallmann, C., Selby, D., 2014. Re-Os geochronology and coupled Os-Sr isotope constraints on the Sturtian snowball Earth. *Proceedings of the National Academy of Sciences*, 111, 51-56.
- Rooney, A.D., Strauss, J.V., Brandon, A.D., Macdonald, F.A., 2015. A Cryogenian chronology: Two long-lasting synchronous Neoproterozoic glaciations. *Geology*, 43, 459-462.
- Rose, C.V., Swanson-Hysell, N.L., Husson, J.M., Poppick, L.N., Cottle, J.M., Schoene, B., Maloof, A.C., 2012. Constraints on the origin and relative timing of the Trezona $\delta^{13}\text{C}$ anomaly below the end-Cryogenian glaciation. *Earth and Planetary Science Letters*, 319-320, 241-250.
- Rose, C.V., Maloof, A.C., Schoene, B., Ewing, R.C., Linnemann, U., Hofmann, M., Cottle, J.M., 2013. The end-Cryogenian glaciation of South Australia. *Geoscience Canada*, 40, 256-293.
- Sarkar, S., Banerjee, S., Smanta, P., Chakraborty, N., Chakraborty, P.P., Mukhopadhyay, S., Singh, A.K., 2014. Microbial mat records in siliciclastic rocks: Examples from four Indian Proterozoic basins and their modern equivalents in Gulf of Cambay. *Journal of Asian Earth Sciences*, 91, 362-377.
- Schieber, J., 1986. The possible role of benthic microbial mats during the formation of carbonaceous shales in shallow Mid-Proterozoic basins. *Sedimentology*, 33, 521-536.
- Schieber, J., Southard, J.B., Schimmelmann, A., 2010. Lenticular shale fabrics resulting from intermittent erosion of water-rich muds – interpreting the rock record in the light of recent flume experiments. *Journal of Sedimentary Research*, 80, 119-128.

- Schrag, D.P., Higgins, J.A., Macdonald, F.A., Johnston, D.T., 2013. Authigenic carbonate and the history of the global carbon cycle. *Science*, 339, 540-543.
- Selleck, B.W., Carr, P.F., Jones, B.G., 2007. A review and synthesis of glendonites (pseudomorphs after ikaite) with new data: assessing applicability as recorders of ancient coldwater conditions. *Journal of Sedimentary Research*, 77, 980-991.
- Shanahan, T.M., Overpeck, J.T., Beck, J.W., Wheeler, C.W., Peck, J.A., King, J.W., Scholz, C.A., 2008. The formation of biogeochemical laminations in Lake Bosumtwi, Ghana, and their usefulness as indicators of past environmental changes. *Journal of Paleolimnology*, 40, 339-355.
- Shearman, D.J., Smith, A.J., 1985. Ikaite, the parent mineral of jarrowite-type pseudomorphs. *Proceedings of the Geologists Association*, 96, 305-314.
- Shields, G.A. 2002. 'Molar-tooth microspar': a chemical explanation for its disappearance ~ 750 Ma. *Terra Nova*, 14, 108-113.
- Shields, G.A. 2005. Neoproterozoic cap carbonates: a critical appraisal of existing models and the plumeworld hypothesis. *Terra Nova*, 17, 299-310.
- Shields, G.A., Stille, P., Brasier, M.D., Atudorei, N.-V., 1997. Stratified oceans and oxygenation of the late Precambrian environments: A post glacial geochemical record from the Neoproterozoic. *Terra Nova*, 9, 218-222.
- Shields-Zhou, G.A., Hill, A.C., Macgabhann, B.A., 2012. Chapter 17 — The Cryogenian Period. In: Gradstein, F. M., Ogg, J. G., Schmitz, M. D., Ogg, G. M., (eds). *The Geologic Time Scale*. Boston: Elsevier, 393-411.
- Simonson, B.M., Carney, K.E., 1999. Roll-up structures: Evidence of in situ microbial mats in Late Archean deep shelf environments. *Palaios*, 14, 13-24.
- Spence, G.H., Le Heron, D.P., Fairchild, I.J., 2016. Sedimentological perspectives on climatic, atmospheric and environmental change in the Neoproterozoic Era. *Sedimentology*,
- Spencer, A.M., 1971. Late Pre-Cambrian Glaciation in Scotland. Geological Society, London, *Memoirs*, 6.
- Sperling, E.A., Wolock, C.J., Morgan, A.S., Gill, B.C., Kunzmann, M., Halverson, G.P., Macdonald, F.A., Knoll, A.H., Johnston, D.T., 2015. Statistical analysis of iron geochemical data suggests limited late Proterozoic oxygenation. *Nature*, 523, 451-454.
- Sutton, M.D., Garwood, R.J., Siveter, David J., Siveter, Derek, J., 2012. Spiers and VAXML; A software toolkit for tomographic visualisation, and a format for virtual specimen interchange. *Palaeontologia Electronica* Article: 15.2.5T.
- Tahata, M., Sawaki, Y., Yoshiya, K., Nishizawa, M., Komiya, T., Hirata, T., Yoshida, N., Maruyama, S., Windley, B.F., 2015. The marine environments encompassing the Neoproterozoic glaciations: Evidence from C, Sr and Fe isotope ratios in the Hecla Hoek Supergroup in Svalbard. *Precambrian Research*, 263, 19-42.
- Trindade, R.I.F., Font, E., D'Agrella-Filho, A.S., Nogueira, A.C.R., Riccomini, C. 2003. Low-latitude and multiple geomagnetic reversals in the Neoproterozoic Puga cap carbonate, Amazon craton. *Terra Nova*, 15, 441-446.
- Veizer, J., 1993. Trace elements and stable isotopes in sedimentary carbonates. In: Reeder, R.J. (ed.) *Carbonates: Mineralogy and Chemistry*. Mineralogical Society of America, Blacksburg, 265-299.
- Wallace, M.W., Hood, A.V.S., Woon, E.M.S., Giddings, J.A., Fromhild, T.A., 2015. The Cryogenian Balcanoona reef complexes of the Northern Flinders Ranges: Implications for Neoproterozoic ocean chemistry. *Palaeogeography, Palaeoclimatology, Palaeoecology*, 417, 320-336.
- Wang, Y., Cheng, H., Edwards, R.L., Kong, X., Shao, X., Chen, S., Wu, J., Jiang, X., Wang, X. and An, Z., 2008. Millennial- and orbital-scale changes in the East Asian monsoon over the past 224,000 years. *Nature*, 451, 1090-1093.
- Waltham, D., 2015. Milankovitch period uncertainties and their impact on cyclostratigraphy. *Journal of Sedimentary Research* 85, 990-998.
- Weedon, G., 2003. *Time-Series Analysis and Cyclostratigraphy*. CUP.
- Westphal, H., Head, M.J., Munnecke, A., 2000. Differential diagenesis of rhythmic limestone alternations supported by palynological evidence. *Journal of Sedimentary Research* 70, 715-725.
- Williams, G.E., Gostin, V.A., McKirdy, D.M., Preiss, W.V., 2008. The Elatina glaciations (Marinoan Epoch), South Australia: Sedimentary facies and palaeoenvironments. *Precambrian Research*, 163, 307-331.
- Zhang, F., Xu, H., Konishi, H., Kemp, J.M., Roden, E.E., Shen, Z., 2012. Dissolved sulphide-catalyzed precipitation of disordered dolomite: Implications for the formation mechanism of sedimentary

- dolomite. *Geochimica et Cosmochimica Acta*, 97, 148-165.
- Zhang, S., Jiang, G., Han, Y., 2008. The age of the Nantuo Formation and Nantuo glaciation in South China. *Terra Nova*, 20, 289-294.
- Zhang, S., Wang, X., Hammarlund, E.U., Wang, H., Costa, M.M., Bjerrum C.J., Connelly, J.N., Zhang, B., Bian, L., Canfield, D.E., 2015. Orbital forcing of climate 1.4 billion years ago. *Proceedings of the National Academy of Sciences*, 112, E1406–E1413, doi: 10.1073/pnas.1502239112.
- Zhou, C., Tucker, R., Xiao, S., Peng, Z., Yuan, X., Chen, Z., 2004. New constraints on the ages of Neoproterozoic glaciations in south China. *Geology*, 32, 437-440.

Table 1: Summary stratigraphy and palaeoenvironments of the Polarisbreen Group, after Hambrey (1982), Halverson (2011) and Benn et al. (2015). Glacigenic units are shown in red and the E3-E4 interval, the subject of this paper, is shown in bold.

Geological System	Group	Formation	Member	Thickness (m)	Lithologies	Interpreted environment
Cryogenian	Polarisbreen	Dracoisen	D1 to D7	465	Cap carbonate passing up into shale then sandstone and mudstone alternations with a central and a capping dolomite unit	Transgressive coastal to offshore, becoming playa lake, then coastal
			Wilsonbreen	W1 to W3	130-180	Diamictites and sandstones with limestone and dolomite units in the W2 and W3 overlying sandstones over brecciated dolomite
		Elbobreen		E4 (Slangen)	20-30	Oolitic dolomite
			E3 (Macdonaldryggen)	200	Finely laminated dolomitic silty shale	Offshore marine
			E2 (Petrovbreen)	10-20	Dolomitic diamictites, rhythmites and conglomerates	Glacimarine
			E1 (Russøya)	75-170	Dolomites overlain by limestone with molar tooth structure, black shale and dolomite	Shallow marine

base at 720 Ma likely to lie in this member

Figure captions

Figure 1. (left) Location of the Svalbard archipelago with the study region shown as a rectangle (enlarged on right) on the main island, Spitsbergen. In the right diagram rock outcrops (nunataks, grey) are surrounded by ice and snow (white). Abbreviations DRA (Dracoisen), DIT (Ditlovtoppen), AND (Andromedafjellet), REIN (informal name, Reinsryggen), BACN (Backlundtoppen-Kvitfjella ridge where a section of upper E3 and E4 is exposed), BACS (South Backlundtoppen, where a section of E2 and basal E3 is exposed).

Figure 2. Stratigraphic profiles through Elbobreen Formation, E3 (Macdonaldryggen Member) and E4 (Slangen Member) at locations shown in Figure 1.

Figure 3. E2-E3 transitional facies containing glaciogenic sediment from Ditlovtoppen (**F**) and south Backlundtoppen (all others). **A.** Thin section of graded rhythmites, 4 m below the top of E2. **B.** Limestone rhythmites sharply overlain by an event bed with sandy base, becoming pebbly upwards (1 m below top of E2). **C.** Polished hand specimen exhibiting prominent diamictite (till) pellet (upper right) and ice-rafted sediment within laminites containing authigenic dolomite (5 cm above base of E3). **D.** Limestone laminites showing sedimentary deformation (same horizon as **B.**) **E.** Thin section of limestone rhythmites (as **B**, **D**) showing microspar laminae with intervening dolomicritic laminae contain sediment grains. Prominent central stylolite. **F.** Precipitated dolomite laminites with dropstones, 5 cm above base of E3. **G**, **H.** Same sample as **C.** in thin section under transmitted light (**G**) and cathodoluminescence (**H**). Detritus is dolomite silt and sand with variable luminescence characteristics, quartz (black) and feldspar (blue) silt. Authigenic dolomite is abundant in the matrix and an early bright cement zone surrounds clasts.

Figure 4. Limestones from South Backlundtoppen, 1 m above the base of E3. **A.** Field photograph with recumbent soft-sediment folds (examples of fold noses are arrowed). **B.** Thin section displaying pale microspar laminae and recumbent fold noses (arrows). **C.** and **D.** transmitted light and cathodoluminescence respectively. Microspar laminae with slightly bulbous tops consist of mosaics of rhombic calcite crystals with a consistent cathodoluminescence zonation indicating simultaneous replacement of a precursor phase.

Figure 5. Dolomitized basal E3 facies, 2.2 m above base of E3, Reinsryggen. **A.** Thin section displaying pale dolomicrospar layers alternating with dolomicrite with soft-sediment folds. **B.** Photomicrograph in transmitted light showing brecciation into “pseudo-allochems” that occurs in the region of fold noses and which creates pore spaces (white) later filled by cement. **C.** and **D.** paired transmitted light and cathodoluminescence photomicrographs showing growth of replacive dolomicrospar crystals with consistent luminescence zonation. **E.** and **F.** paired transmitted light and cathodoluminescence photomicrographs showing replacive dolomicrospar of “pseudo-allochems” passing into clear, non-luminescent dolomite cement.

Figure 6. Oxygen and carbonate isotope plot of E3 and E4 samples.

Figure 7. Stratigraphic variation in sediment chemistry around the E2-E3 transition and lower E3. Carbon isotopes show a steady rise from the base of the formation. Extreme variability is restricted to the basal bed. Reinsryggen dolomites have less negative values than other sites at the same stratigraphic position. Insoluble residue and Fe display parallel trends (mirrored as plotted) with an initial decrease corresponding to purer carbonates, followed later by an increase to the mixed carbonate-siliciclastic sediment characteristic of the bulk of E3.

Figure 8. Rhythmic sedimentation in member E3. **A.** Dracoisen section viewed from the south, starting with beginning of exposure approximately 40 m above the base of E3. Double yellow lines show direction of bedding. Flat-topped hill to right is unconformable Carboniferous cover. **B.** Enlargement of boxed area in (**A**) illustrating variable degree of expression of sedimentary rhythms. **C.** Two orange-weathering dolostone horizons, the upper one of which wedges out to right of the 35 cm hammer (ca. 150 m above base of Ditlovtoppen section). **D.** Non-resistant part of rhythm (93.8 m, Dracoisen); height of view 45 cm. **E.** Resistant part of rhythm (97.4 m, Dracoisen); height of view 45 cm. **F.** Distinctly concretionary dolostone horizon containing sedimentary layers that thin by a factor of two laterally into dolomitic shale (42 m; Dracoisen section); ruler 19 cm long.

Figure 9. Transmitted light petrography of dolomitic silt-shales from the main part of E3 in the Dracoisen section. **A-C.** scale is in millimetres. **A.** Sample with relatively high (60%) carbonate content forming dolomite- and calcite-cemented concretion at 42.75 m). Lamination is parallel, but micro-nodular on sub-millimetre scale. **B.** Sample with 50% carbonate (dolomite >> calcite) consisting of carbonate domains with fine silt separated by clay-rich laminae that show complex deformation (disturbance structures) at 67 m. **C.** Sample containing 70% dolomite and also rich in quartzo-feldspathic silt (187 m) showing incipient cross-lamination and very thin lenses of coarser silt; such silt-rich sediments are only found in the E3-E4 transition zone. **D** and **E.** Same sample as in **(A)** illustrating discontinuous clay-pyrite flaser laminae separated by domains of fine silt with carbonate. **F.** Same sample as **(B)** illustrating deformed laminae. **G.** Sample with 35-40% carbonate (dolomite) with much siliciclastic silt and distinct deformed clay-rich laminae, 106.9 m. **H.** Sample with 30% carbonate as dolomite with abundant fine-medium siliciclastic silt, 173 m.

Figure 10. Disturbance structures. **A-C.** Bedding plane outcrop views. **A.** Typical equant structures 1-2 cm across, Dracoisen 65 m. **B.** Close-up of two structures with deformed laminae visible (width of photo 3 cm), Ditlovtoppen, 40 m. **C.** Linear array of structures, Dracoisen, 65 m. **D-F.** Vertical cross-sections. **D.** Smoothly weathered outcrop with disturbance structure bounded above and below by undisturbed lamination, Klofjellet, exact stratigraphic position unknown. **E.** Weathered outcrop showing several structures vertically offset from each other (mm scale at lower left), Dracoisen, 45 m. **F.** Polished surface of sample used for serial sections, Dracoisen, 53 m. **G-J.** Computer model from serial sectioning of sample shown in **(F)**; lettering indicates snapshot from movie in supplementary information. **G.** Conical core to structure seen in vertical section. **H.** As **(G)** rotated through 90° and displaying double-pointed termination. **I.** As **(H)**, but also showing enclosing (red) lamina. **J.** Complete model seen from reverse side with sheath-like laminae in the core and continuous overlying green lamina overlain by further deformed laminae.

Figure 11. Trains of disturbance structures from Klofjellet (exact horizon unknown). **A.** Cut hand specimen displaying continuous lamination interrupted by various structures including a train climbing from 1 to 3. A pale lamina at 2 is nearly undisturbed across the train. **B-C.** Model from 31 serial sections (totalling 0.62 mm depth) of the lower right portion of the sample. **B.** View of model from front of slab showing tubular nature of structures (cf. **A**). **C.** Transverse view of model with front at arrowhead to right, illustrating narrowing of structures into the slab on left of image. **D.** Another cut from same sample illustrating both disturbance structures and brittle failure (e.g. arrowed). Examples of local variations in lamina thickness are numbered. Diagonal lines are saw marks.

Figure 12. Stratigraphic variation within E3 of carbonate stable isotope values. Key as in Fig. 6.

Figure 13. Stratigraphic variation within E3 of % insoluble residue (non-carbonate) and acid-soluble Fe, expressed as FeCO_3 . Key as for Fig. 6.

Figure 14. E3 samples from Dracoisen section view under CL (**A-C**) and by BSE (**D-F**). **A.** Sample at 48.7 m with 40-45% carbonate (dolomite>>calcite). Siliciclastic silt includes quartz (dark), feldspar (blue) and apatite (green). Zonation is inconsistent between dolomite crystals, i.e. they did not grow simultaneously. **B.** Sample at 46.55 m with 45% carbonate (dolomite). Similar to **(A)** but with more segregation of quartzo-feldspathic detritus and dolomite into laminae. **C.** Sample at 68.55 m with 50% carbonate (subequal dolomite and calcite). Finer texture than **(A)** and **(B)** with fine-to-medium quartz silt and heterogenous zonation in carbonate crystals. **D.** Sample at 42.75 m with 60% carbonate (subequal dolomite and calcite), visibly concretionary in the field (Fig. 8F). Dolomite crystals tend to be isolated and enclosed by calcite. **E.** and **F.** Sample at 177 m with 30% carbonate (dolomite). Dolomite forms subhedral crystals with brighter (more Fe-rich) rims; calcite tends to show more irregular or enclosing shapes; pyrite framboids are conspicuous. C = calcite, D = dolomite, F = feldspar, P = pyrite, Q = quartz.

Figure 15. Ion microprobe data (full data in Supplementary information, Table S2) from individual carbonate crystals performed by downward ablation of carbonate crystals to 100 μm depth in 5 μm steps. Analyses are thus biased towards crystal centres and no information is available about relative age of zones. **A.** Example of sample F7163 (42.75 m, Dracoisen) where points joined with lines are depth traverses of single crystals. Overall there is overlap in chemistry of dolomite and calcite with orders of magnitude variation in abundance, and

tendency for variation in Fe or both Fe & Mn within individual crystals. B. comparison of means of dolomite and calcite crystals from ion microprobe analysis with ICP data for acid-soluble Fe and Mn, both expressed as wt.% carbonate. ICP means are high in Fe due to some leaching of Fe from silicate phases. Samples are from Dracoisen section at the following stratigraphic positions: 109 (48.3 m, see also Figs. 9A, D, E, 14D), F7199 (106.9 m, see also Fig. 9G), F7182 (68.55 m, see also Fig. 14C), F7163 (42.75 m), F7266 (177.0 m, see also Fig. 14E, F).

Figure 16. Sedimentary rhythms within member E3. A. Comparison of cumulative thickness of individual cycles at the Dracoisen and Ditlovtoppen localities. B. and C. Histograms of cycle thickness at the Dracoisen and Ditlovtoppen locations (numbers beneath bins indicate upper end of bin range).

Figure 17. Geochemistry of E3 rhythmic sediments from the Dracoisen section. A. and B. show results from Principal Components Analysis of XRF and ICP data respectively. The diagrams display the weighting on the first principal component (F1) on the x-axis, together with the % of data variation, plotted against F2 on the y-axis. In both case Ca provides the best indicator of sample variation, mapping nearly perfectly onto F1. C. Variation of Ca in total sample (ICP analysis) from a detailed sampling section through seven field-defined rhythms (XRF data are not plotted, but are very similar). The intensively sampled harder bed at around 45.5 m is enriched in Ca, but at higher levels there is a lack of clear relationship with rhythms. D. Variation of Ca in total sample (ICP analysis) from higher horizons in E3 in the Dracoisen section. At most horizons there is a lack of systematic difference in Ca content between the field-defined lithologies.

Figure 18. Phenomena around the E3-E4 transition. A. Polished hand specimen illustrating dolomitic siltstones with distinct coarser and finer (dark) laminae and common 2-3 mm vugs representing crystal pseudomorphs. Scale bar in cm; 9 m below top of E3, Dracoisen. B. Silty laminated dolarenites with ripple-laminated thin graded units and ptymatically folded sediment-filled contraction cracks. 2 m above base of E4, Reinsryggen. C. Dolomitic siltstone with dark-coloured elongated mudclasts and abundant crystal pseudomorphs, some open, some filled by calcite with minor quartz. 0.5 m below the top of E3, Reinsryggen. D. Same sample as (C) illustrating diagenetic quartz containing anhydrite inclusions (e.g. arrowed). E. Fine-grained dolarenites containing nodular vuggy pseudomorphs now composed of quartz (white) or ferroan dolomite (orange). Scale bar in cm, base of E4, Ditlovtoppen. F. Same sample as (E) illustrating anhydrite inclusions (e.g. arrowed) in diagenetic quartz.

Figure 19. Strontium isotope data from E3 limestones in Backlundtoppen sections. A. $^{87}\text{Sr}/^{86}\text{Sr}$ versus Sr. B. $^{87}\text{Sr}/^{86}\text{Sr}$ versus Mn/Sr.

Supplementary data

Supplementary data Table S1. Stable isotope, Sr isotope, ICP and magnetic susceptibility data

Supplementary data Table S2. Ion microprobe data

Supplementary data Table S3. X-ray fluorescence data

Supplementary data Table S4. Zircon data from NIGL.

Supplementary data Table S5. Zircon data from Adelaide laboratory.

Supplementary Video 1: “3 loops.avi” from three-dimensional computer model derived from sample illustrated in Figure 11.

Supplementary Video 2: “core.avi” from three-dimensional computer model derived from sample illustrated in Figure 11.

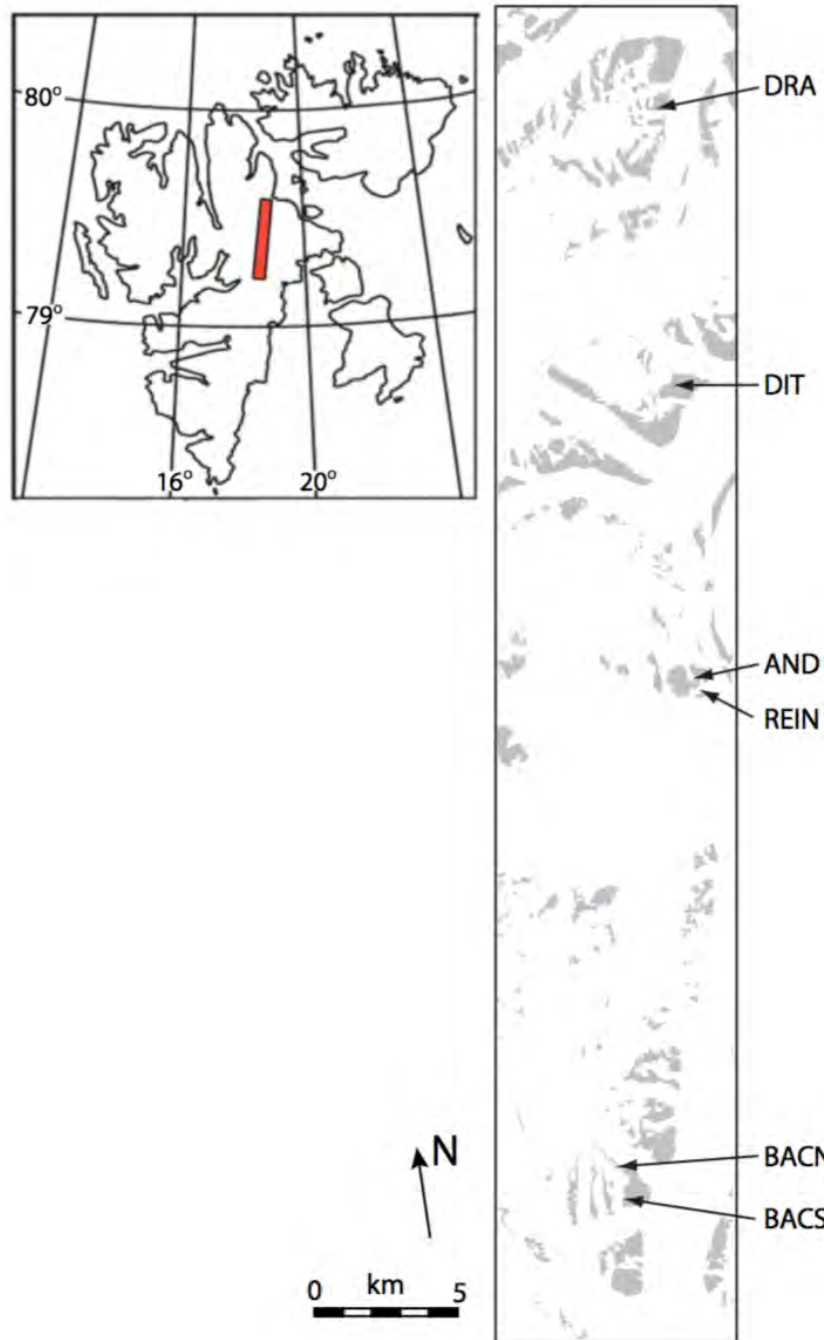


Figure 1

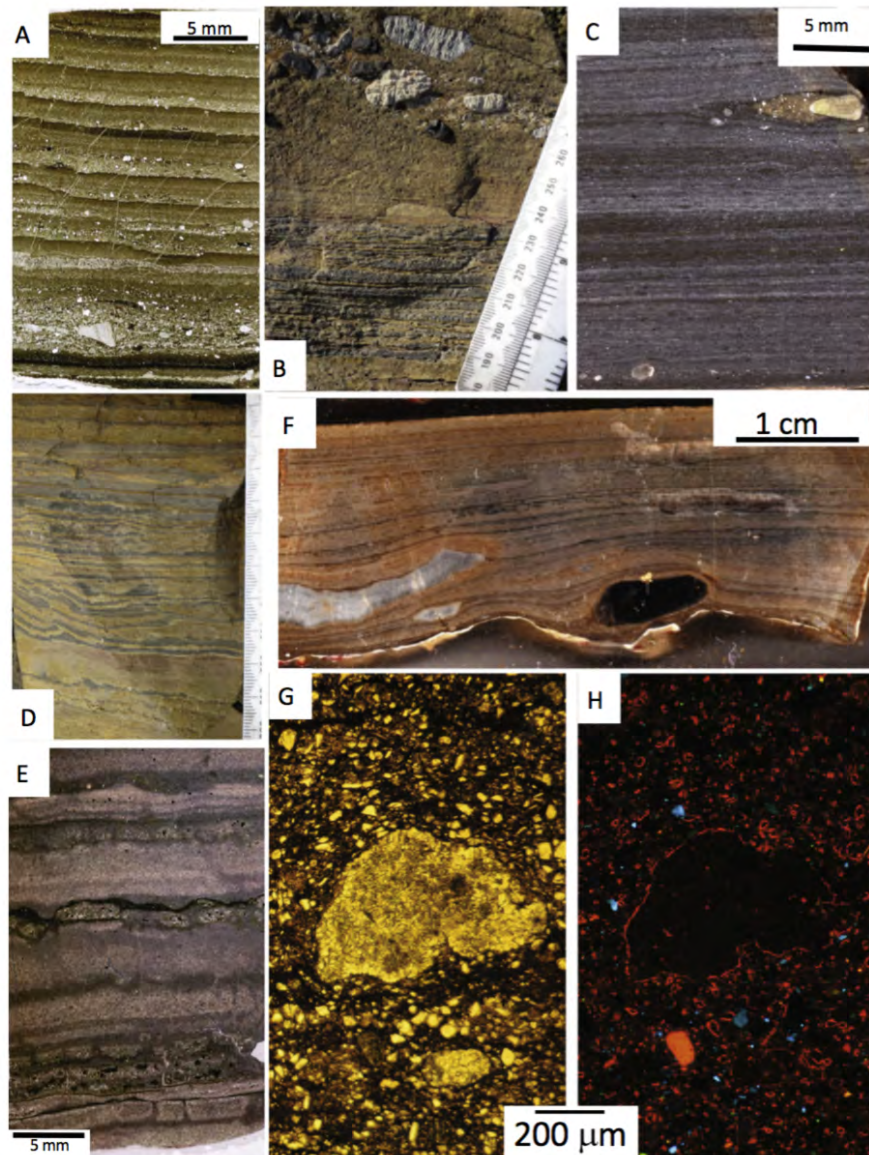


Figure 3

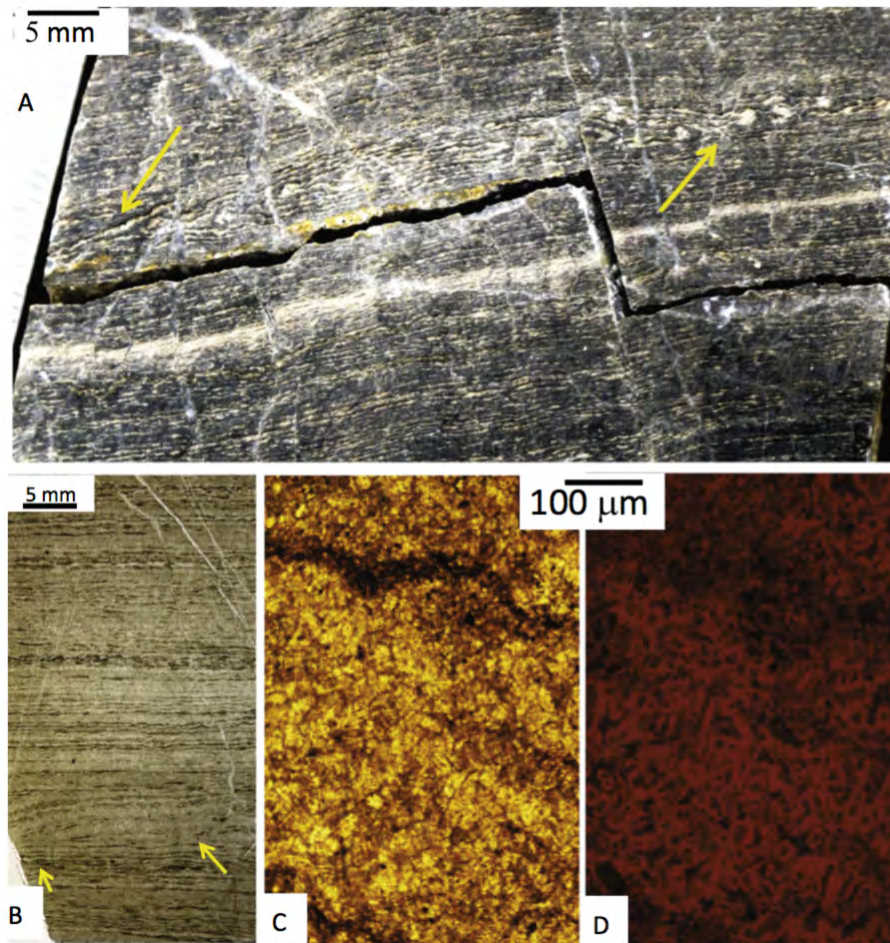


Figure 4

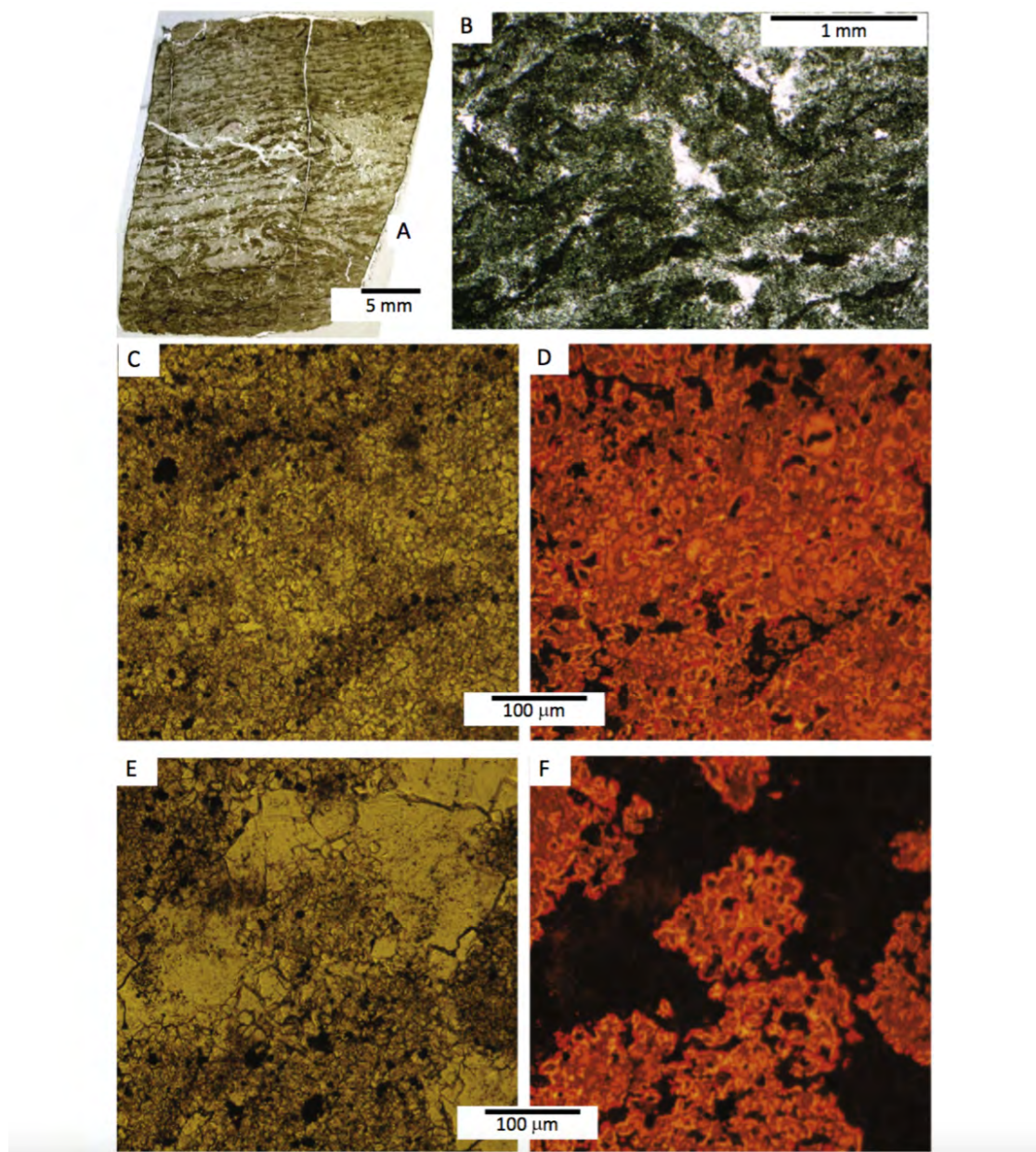


Figure 5

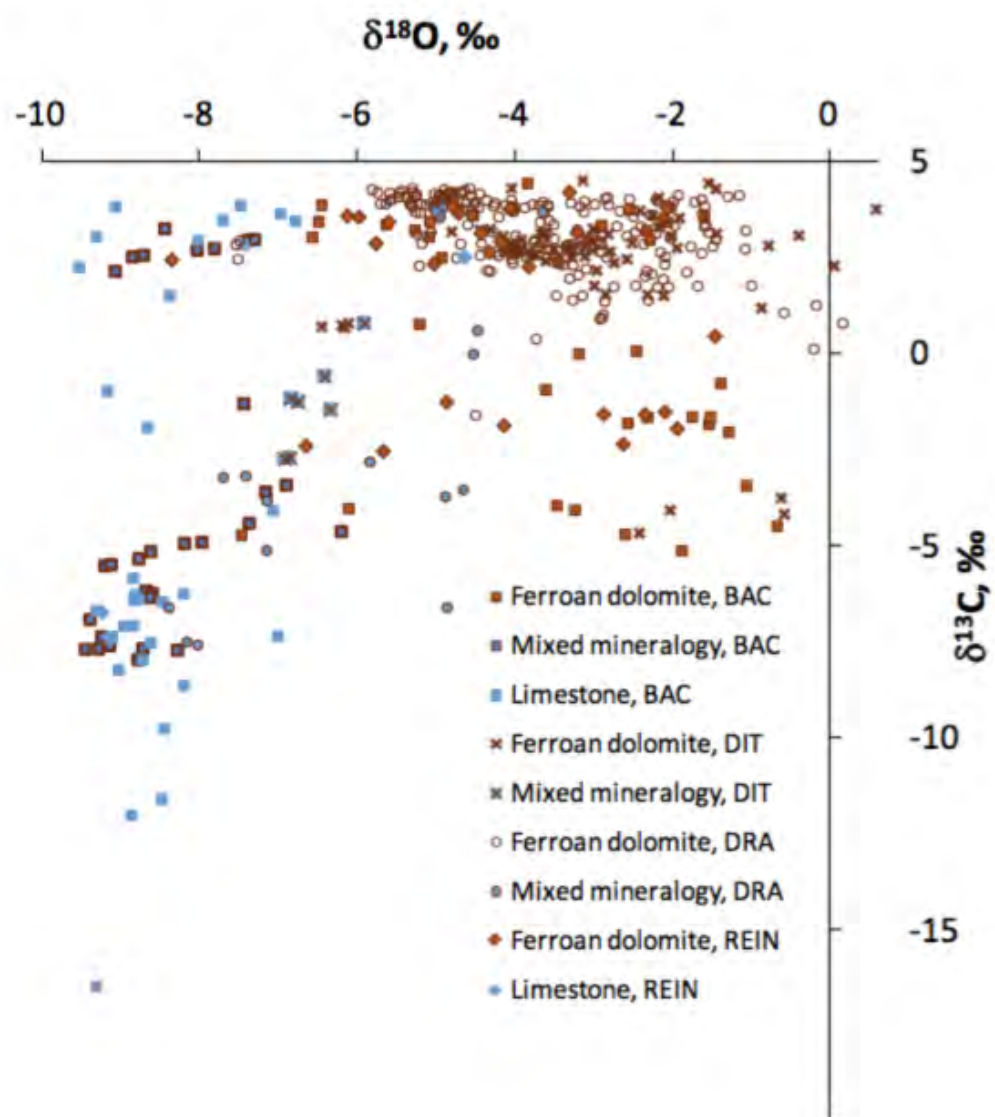


Figure 6

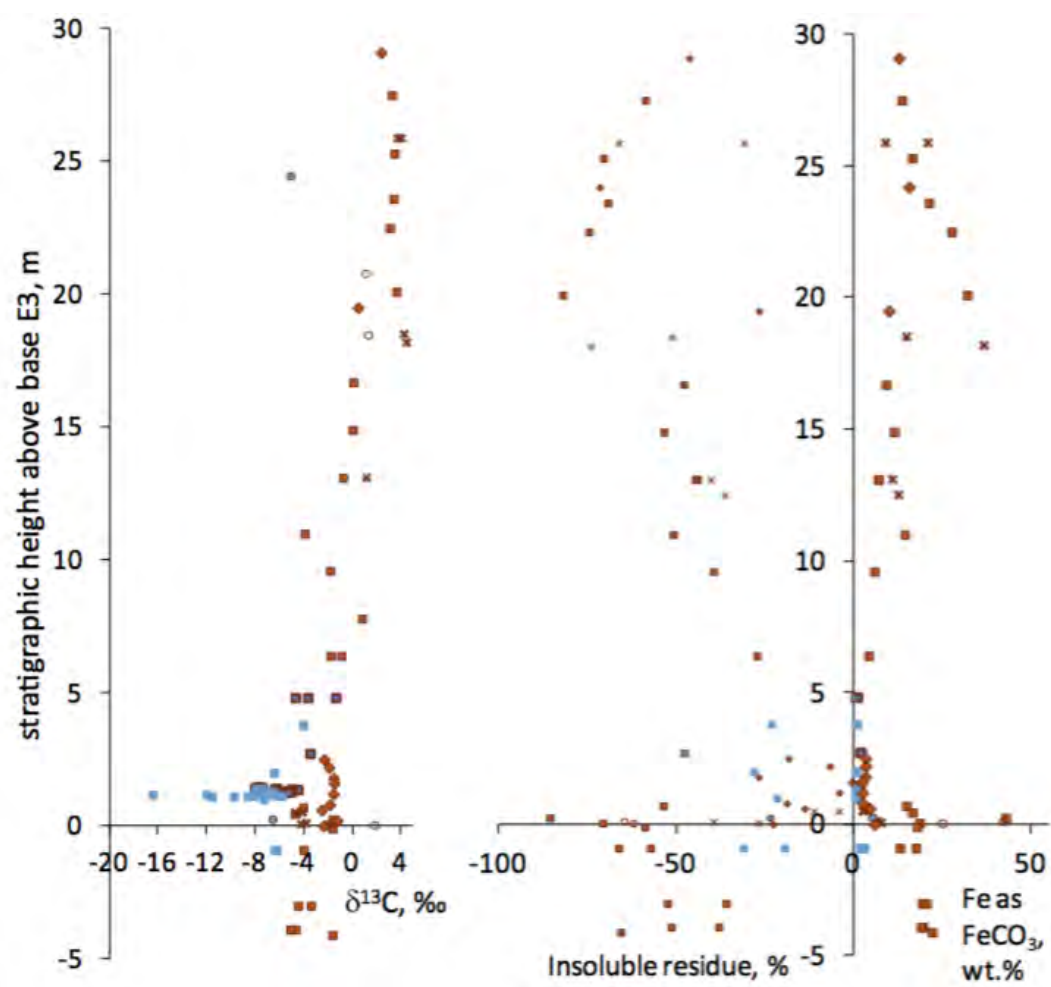


Figure 7

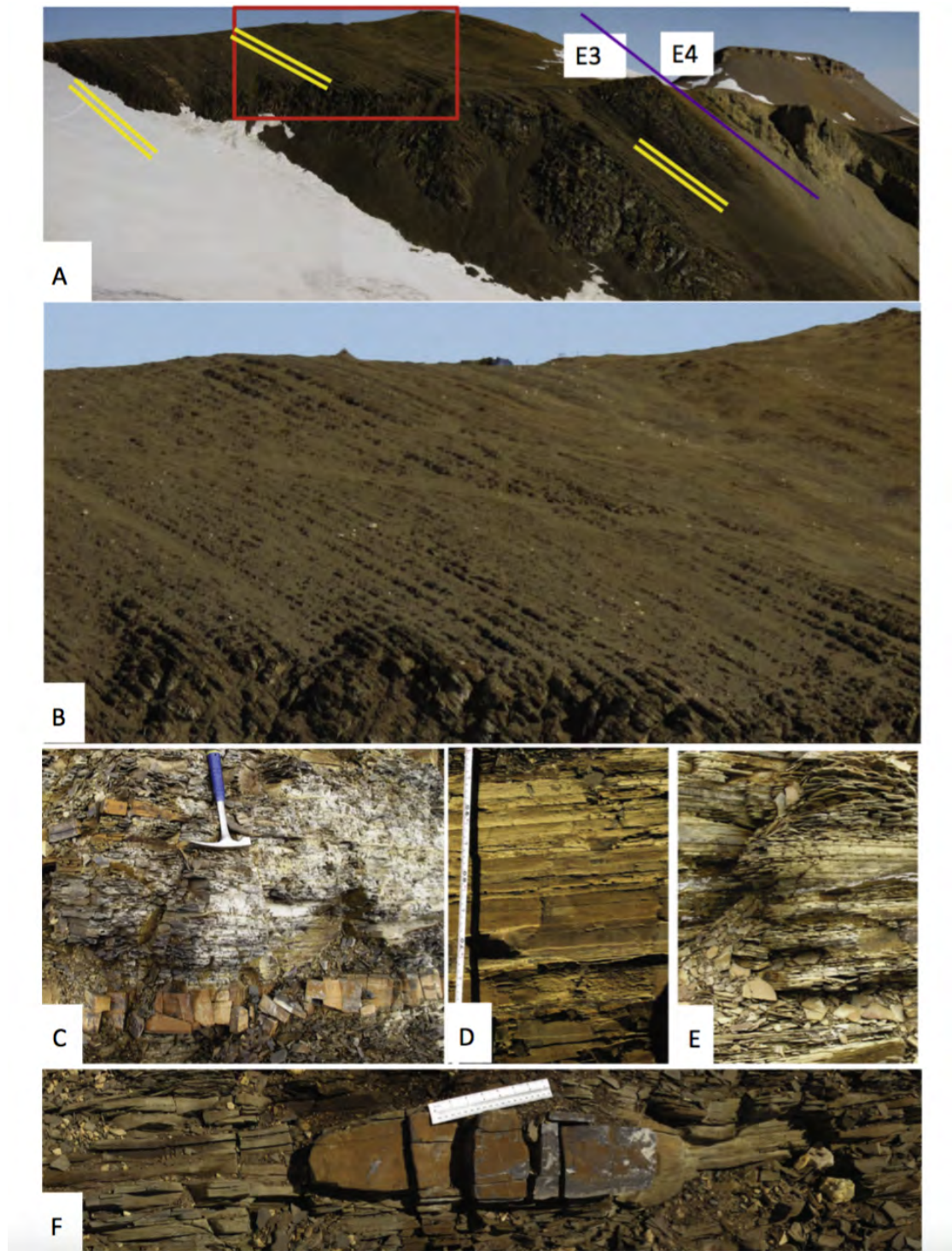


Figure 8

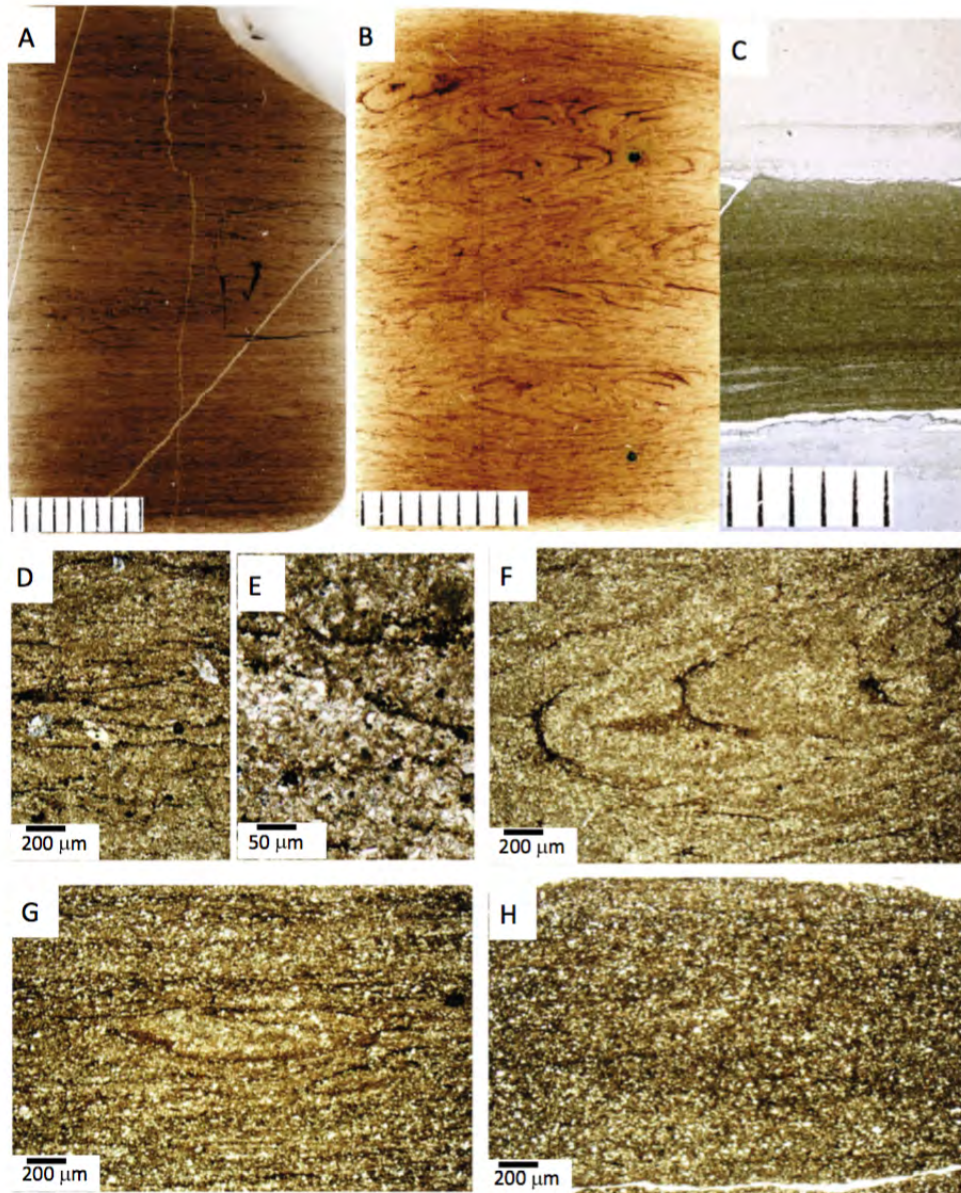


Figure 9

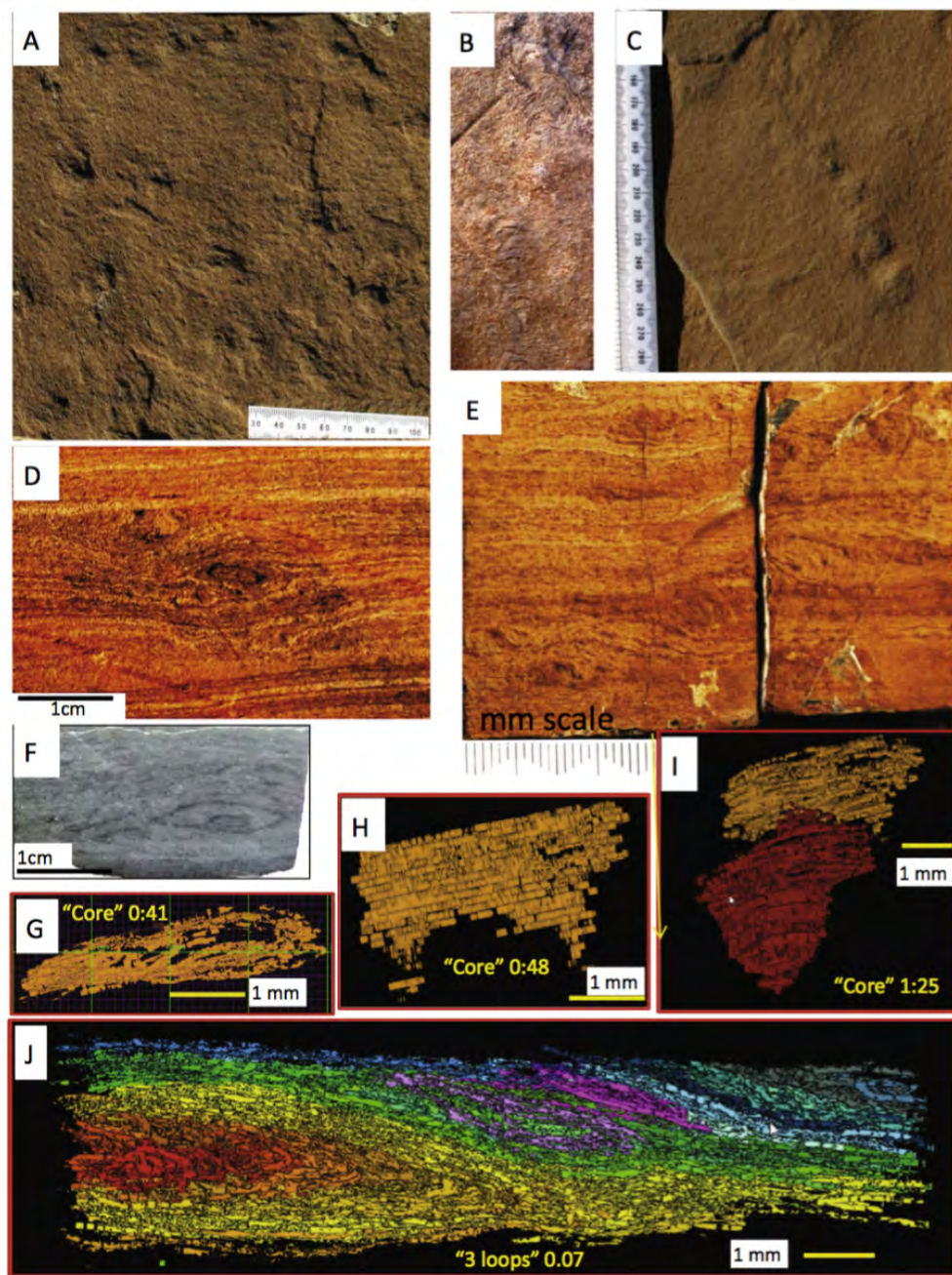


Figure 10

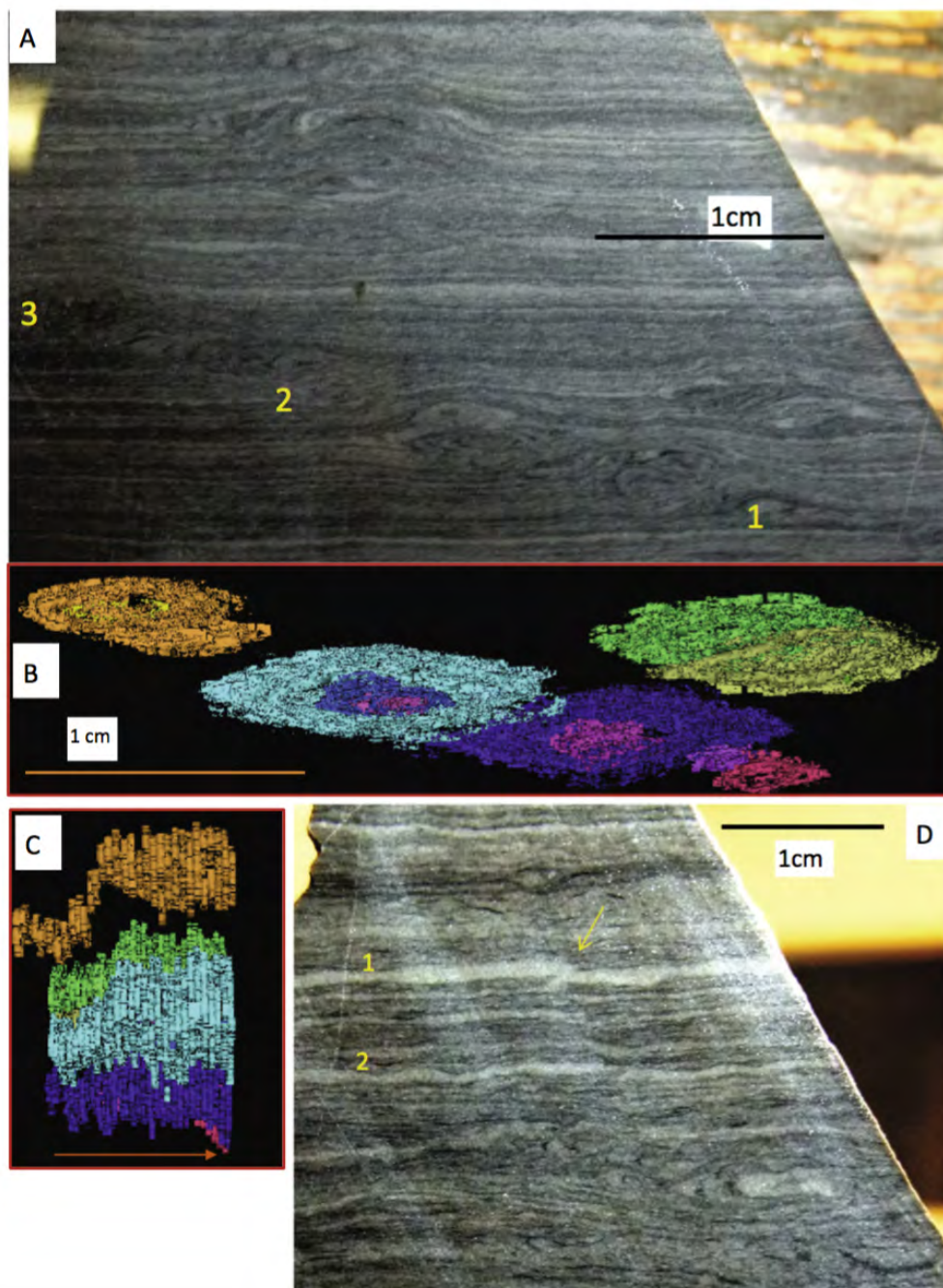


Figure 11

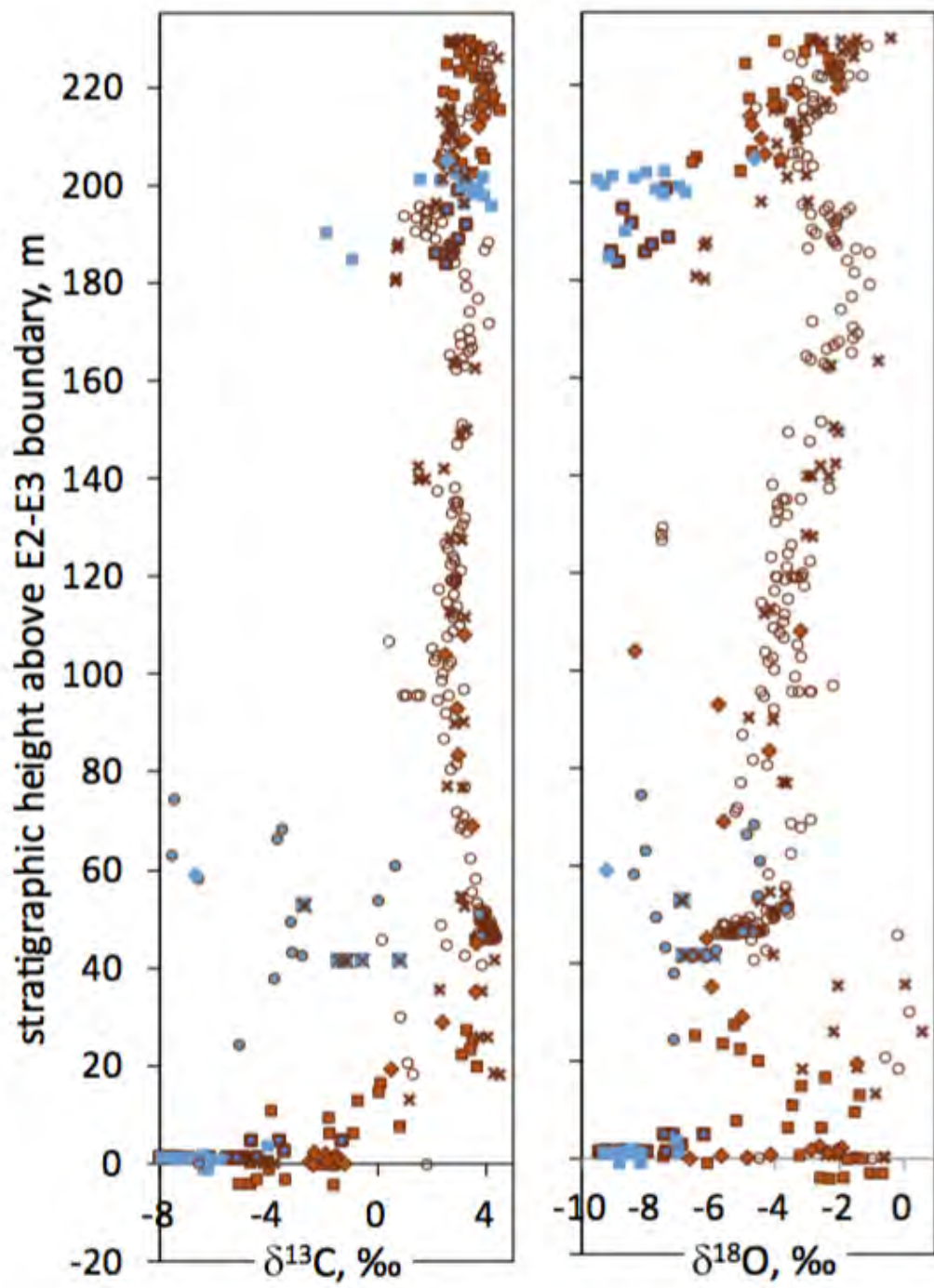


Figure 12

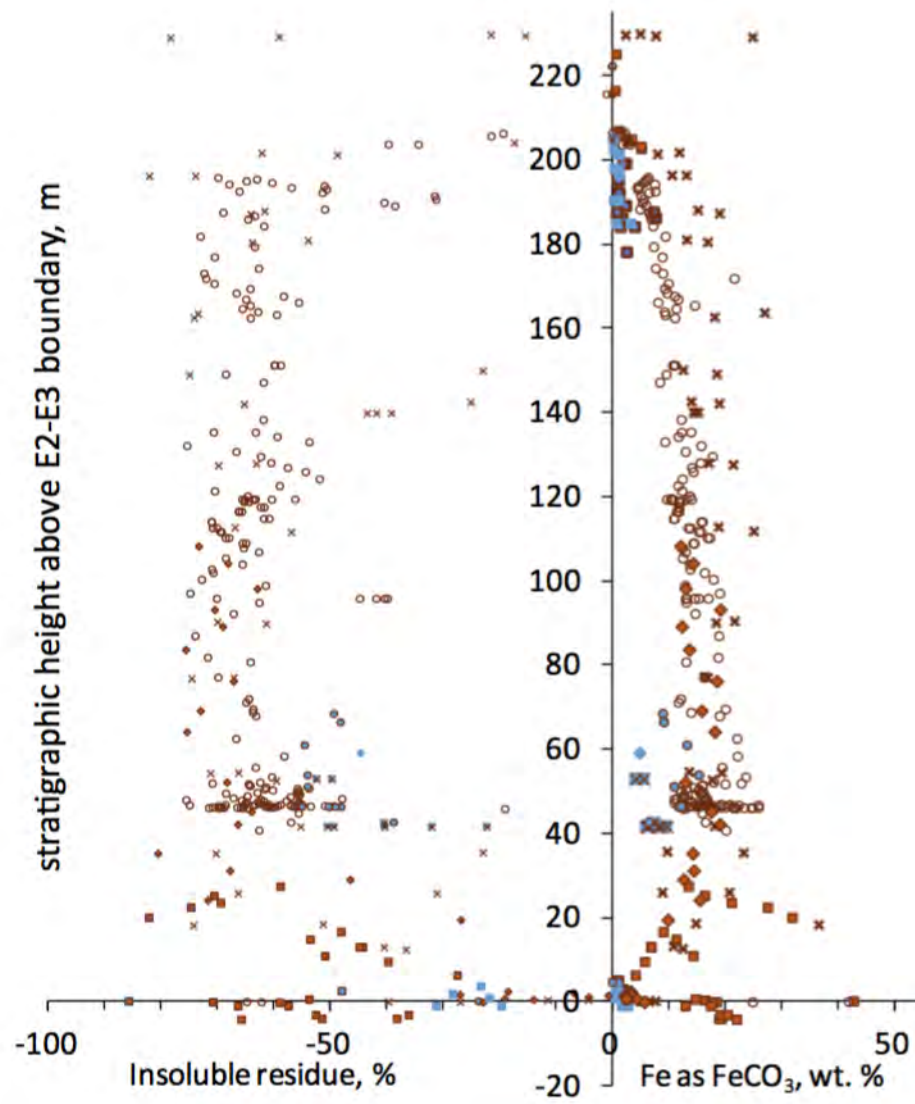


Figure 13

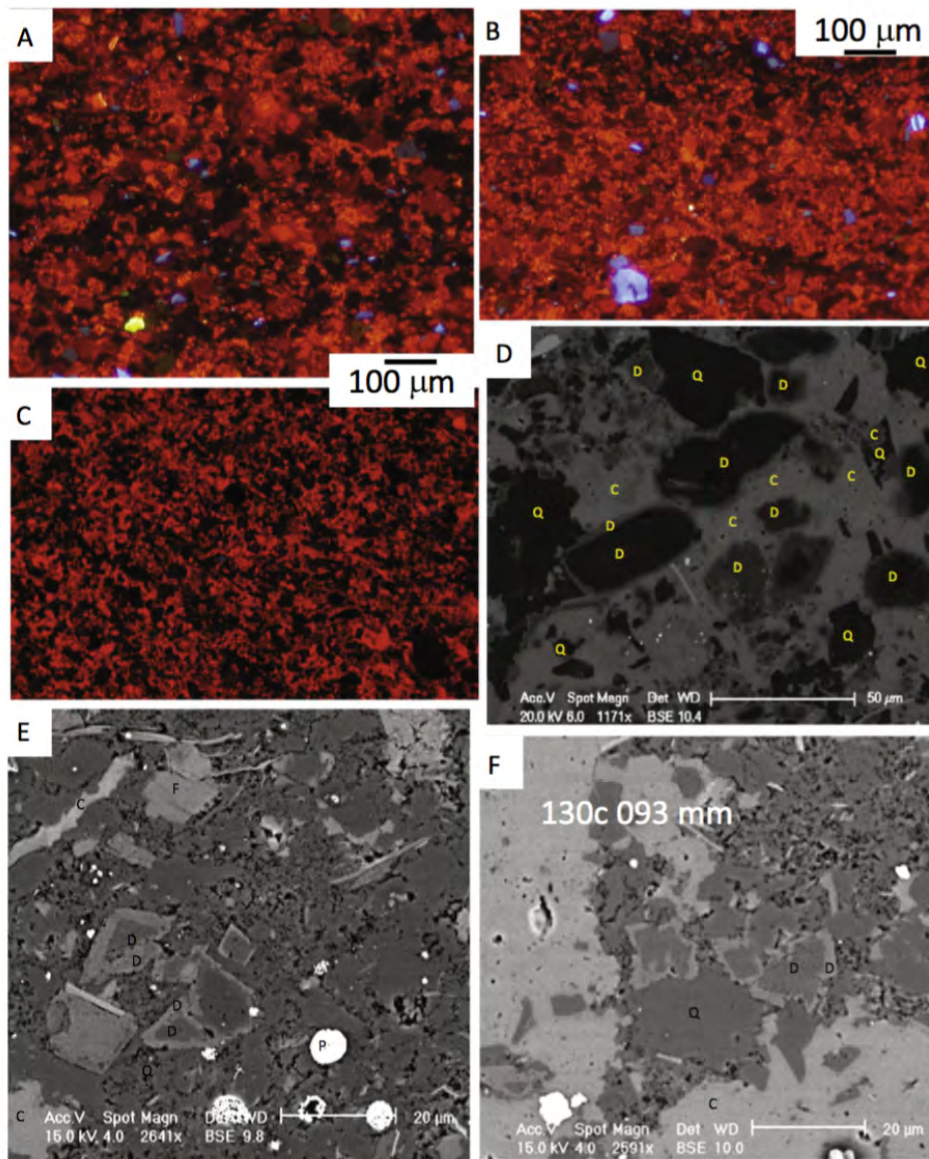


Figure 14

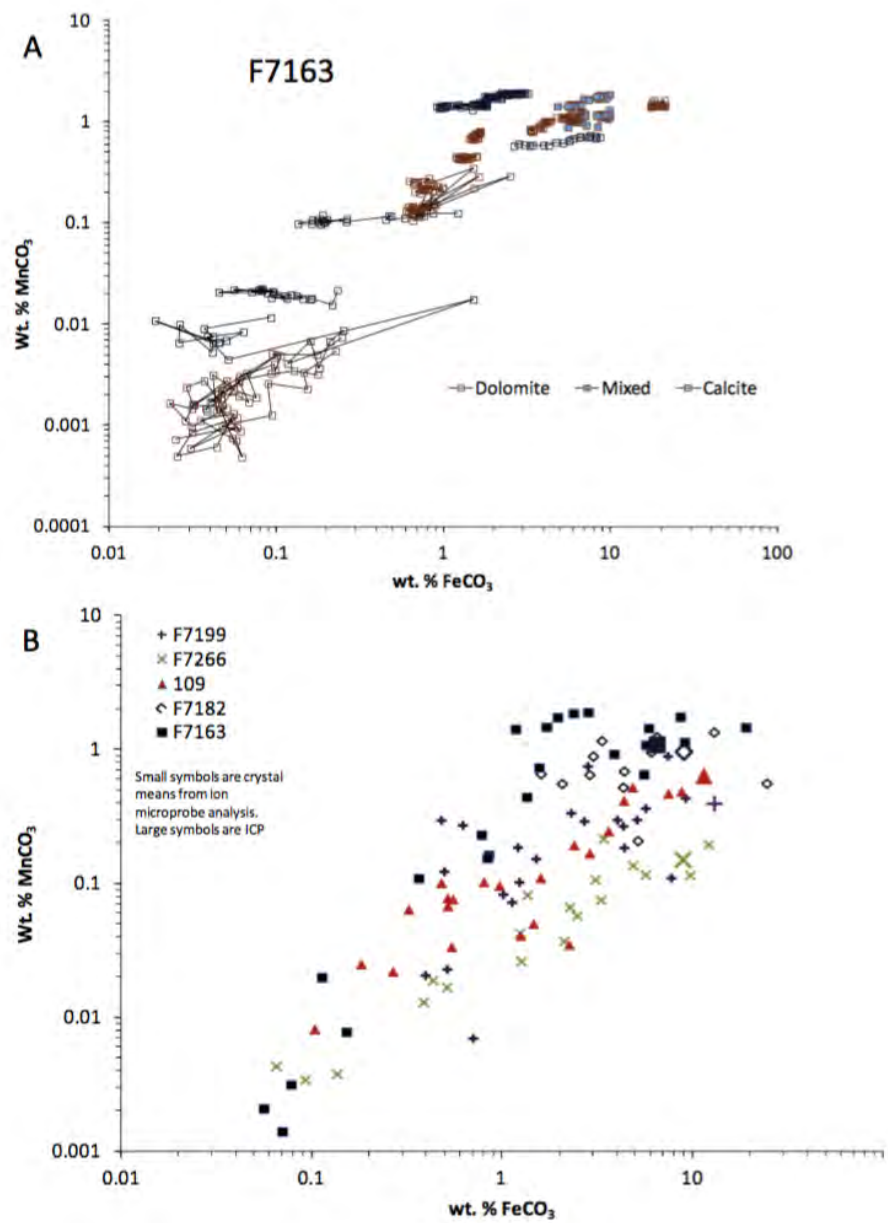


Figure 15

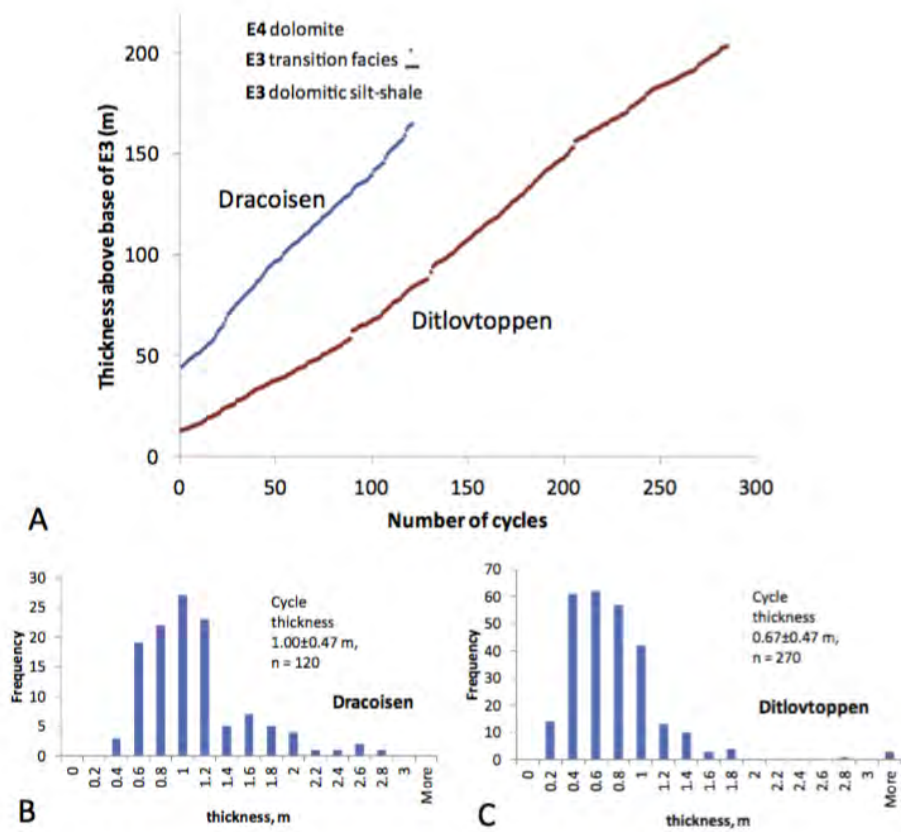


Figure 16

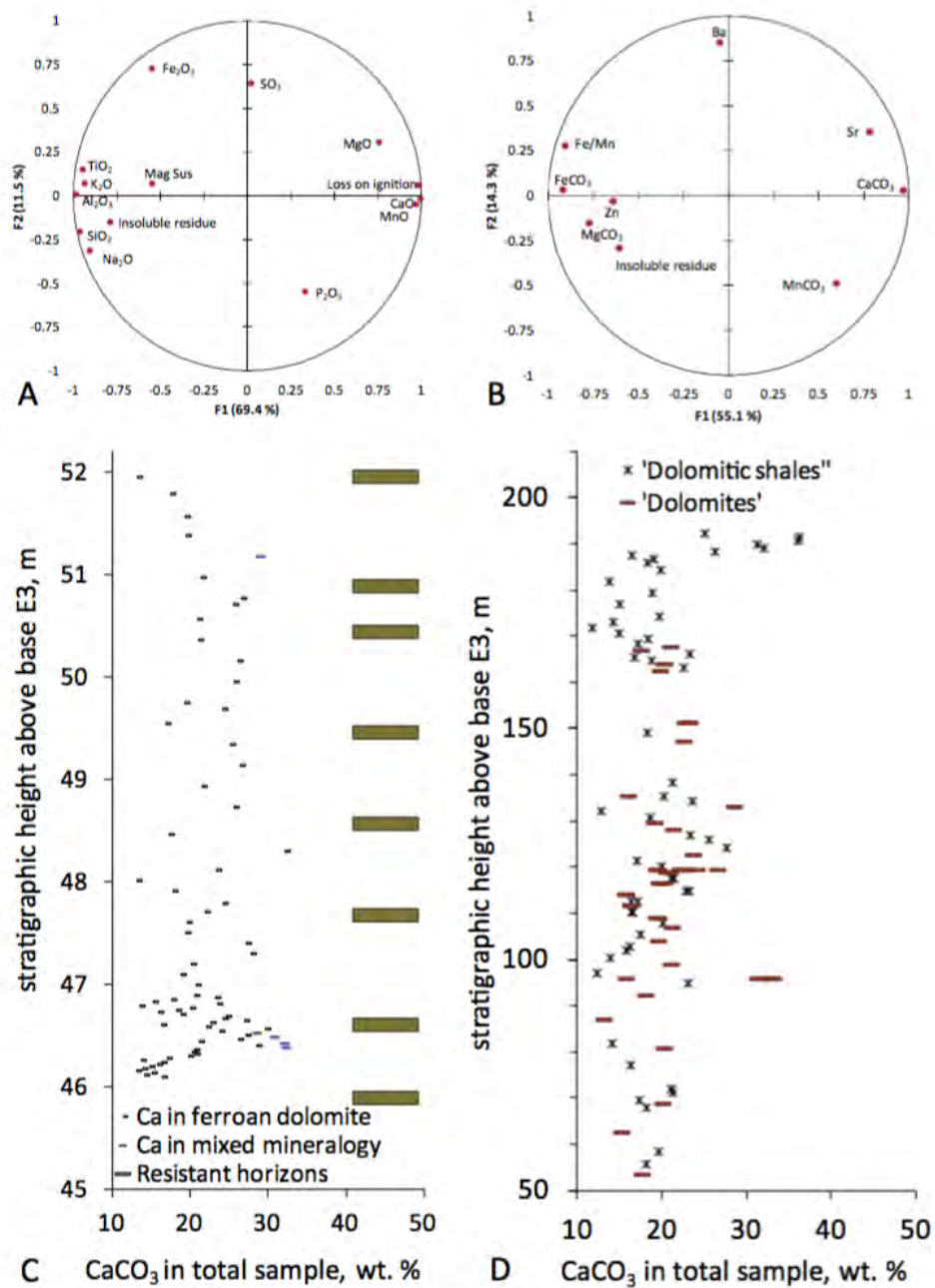


Figure 17

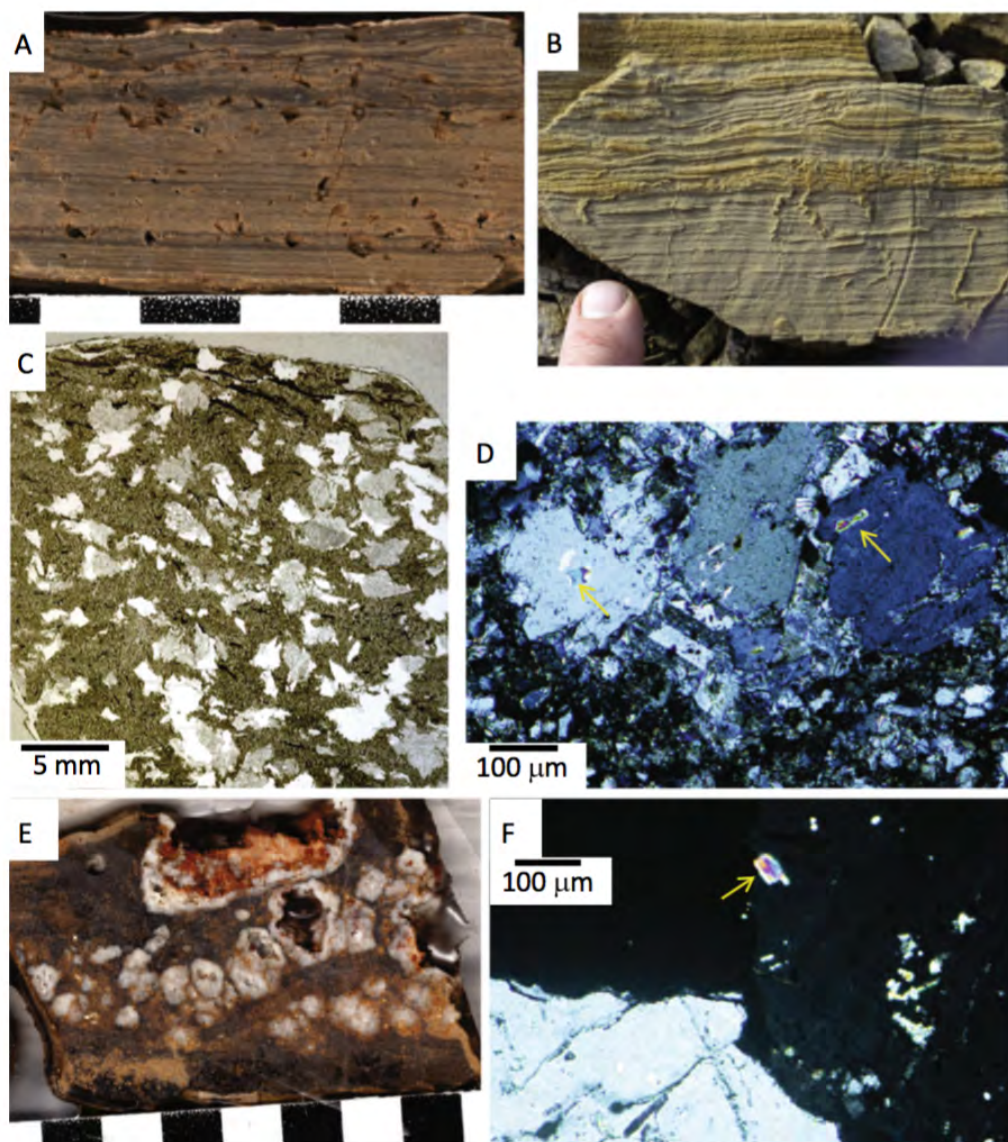


Figure 18

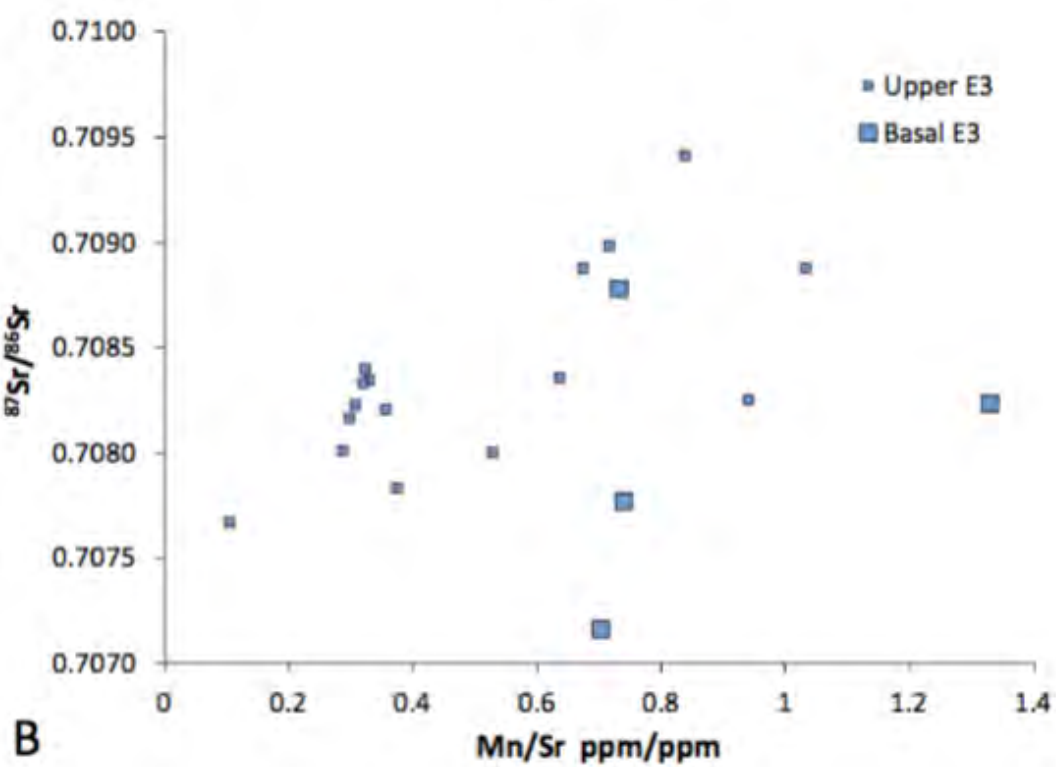
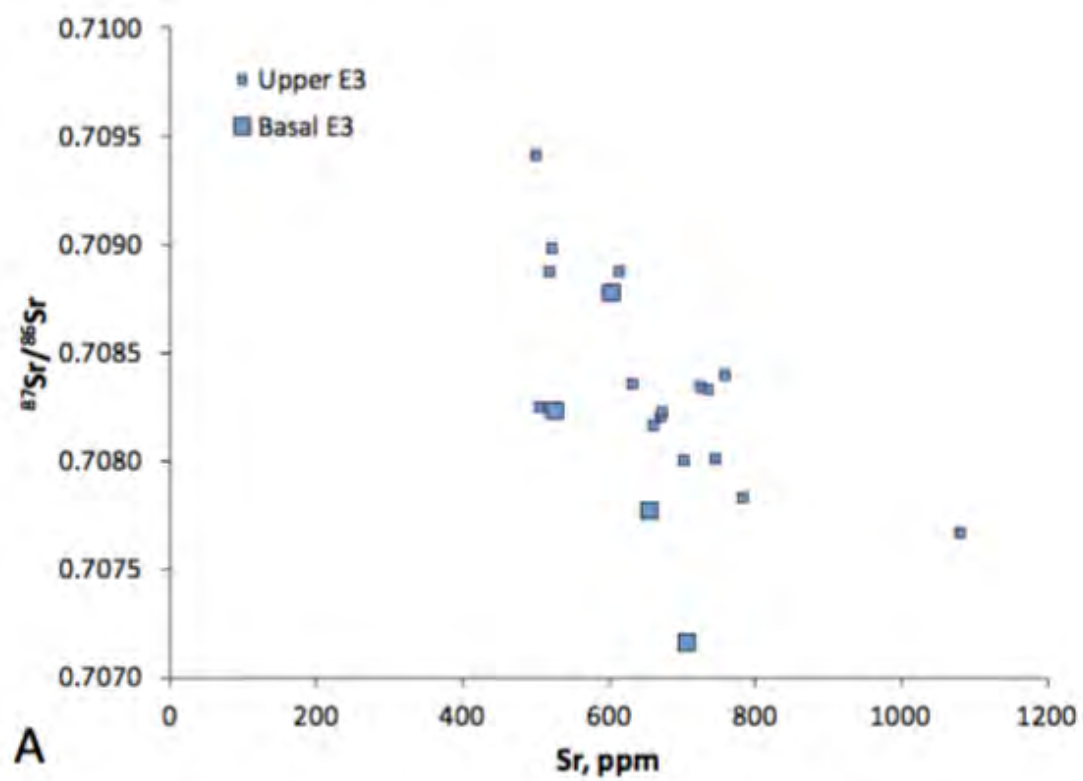


Figure 19